DUNE LBL Physics Paper

DUNE Collaboration

The Deep Underground Neutrino Experiment (DUNE) collaboration has performed sensitivity studies based on full, end-to-end simulation, reconstruction, and event selection of far detector Monte Carlo and parameterized analysis of near detector Monte Carlo. Detailed uncertainties from flux, the neutrino interaction model, and detector effects have been included in the analysis. Sensitivity results are obtained using a sophisticated, custom fitting framework. We present sensitivity to DUNE's goals of measuring the charge-parity violating parameter $\delta_{\rm CP}$ to high precision, unequivocally determining the neutrino mass ordering, and making precise measurements of the parameters governing long-baseline neutrino oscillation. We also present studies demonstrating the necessity of a highly capable DUNE near detector.

PACS numbers:

I. INTRODUCTION

The Deep Underground Neutrino Experiment (DUNE) is a next-generation, long-baseline neutrino oscillation experiment, designed to be sensitive to ν_μ to ν_e oscillation. The experiment consists of a high-power, broadband neutrino beam and a near detector located at Fermi National Accelerator Laboratory, in Batavia, IL and a massive, liquid-argon TPC far detector located at the 4850L of Sanford Underground Research Facility (SURF), in Lead, South Dakota, USA. The neutrino beam is produced using protons from Fermilab's Main Injector and a traditional horn-focusing system. The polarity of the focusing magnets may be reversed to produce a neutrino- or anti-neutrino-dominated beam. A highly capable near detector will constrain systematic uncertainty for the oscillation analysis. The 40-kt (fiducial) far detector is composed of four non-identical, 10 kt (fiducial) LArTPC modules. The baseline of 1285 km provides sensitivity to all parameters governing long-baseline neutrino oscillation in a single experiment. The deep underground location of the far detector facilitates sensitivity to nucleon decay and low-energy neutrino detection, specifically observation of neutrinos from a core-collapse supernova. The experiment plans to begin collecting physics data in 2026. Details of the experimental concept have been described in [1–3]; detector details that are needed to understand the analysis presented here are provided in the following sections. This paper presents updated studies of DUNE sensitivity to the physics governing long-baseline neutrino oscillation.

DUNE plans to pursue a detailed study of neutrino mixing, resolve the neutrino mass ordering, and search for charge-parity symmetry violation (CPV) in the lepton sector by studying the oscillation patterns of high-intensity ν_μ and $\bar{\nu}_\mu$ beams measured over a long baseline. The entire complement of neutrino experiments to date has measured five of the neutrino mixing parameters [4–6]: the three mixing angles θ_{12}, θ_{23}, and θ_{13}, and the two mass differences Δm^2_{21} and $|\Delta m^2_{31}|$. The neutrino mass ordering (i.e., the sign of Δm^2_{31}) is unknown. The values of θ_{12} and θ_{23} are large, while θ_{13} is smaller. The value of $\delta_{\rm CP}$ is not well known, though neutrino oscillation data are beginning to provide some information on its value [7, 8].

The oscillation probability of $\nu_\mu \to \nu_e$ through matter in a constant density approximation is, to first order [9]:

$$\begin{aligned} P(\nu_\mu \to \nu_e) \simeq\ & \sin^2\theta_{23}\sin^2 2\theta_{13}\frac{\sin^2(\Delta_{31}-aL)}{(\Delta_{31}-aL)^2}\Delta^2_{31} \\ & + \sin 2\theta_{23}\sin 2\theta_{13}\sin 2\theta_{12}\frac{\sin(\Delta_{31}-aL)}{(\Delta_{31}-aL)}\Delta_{31} \\ & \times \frac{\sin(aL)}{(aL)}\Delta_{21}\cos(\Delta_{31}+\delta_{\rm CP}) \\ & + \cos^2\theta_{23}\sin^2 2\theta_{12}\frac{\sin^2(aL)}{(aL)^2}\Delta^2_{21}, \end{aligned} \tag{1}$$

where $\Delta_{ij} = \Delta m^2_{ij} L/4E_\nu$, $a = G_F N_e/\sqrt{2}$, G_F is the Fermi constant, N_e is the number density of electrons in the Earth, L is the baseline in km, and E_ν is the neutrino energy in GeV. Both $\delta_{\rm CP}$ and a switch signs in going from the $\nu_\mu \to \nu_e$ to the $\bar{\nu}_\mu \to \bar{\nu}_e$ channel; i.e., a neutrino-antineutrino asymmetry is introduced both by CPV ($\delta_{\rm CP}$) and the matter effect (a). The origin of the matter effect asymmetry is simply the presence of electrons and absence of positrons in the Earth. The electron neutrino appearance probability is shown in Figure 1 at a baseline of 1300 km as a function of neutrino energy for several values of $\delta_{\rm CP}$.

The rich oscillation structure that can be observed by DUNE will enable precision measurement in a single experiment of all the mixing parameters governing ν_1–ν_3 and ν_2–ν_3 mixing. DUNE is designed to make significant contributions to the completion of the standard three-flavor mixing picture. Scientific goals are definitive determination of the neutrino mass ordering, definitive observation of CP violation for more than 50% of possible true $\delta_{\rm CP}$ values, and precise measurement of oscillation parameters, particularly $\delta_{\rm CP}$, $\sin^2 2\theta_{13}$, and the octant of $\sin^2\theta_{23}$. There is great value in obtaining this set of measurements in a single experiment using a broadband beam, so that the oscillation pattern may be clearly observed and a detailed test of the three-flavor neutrino

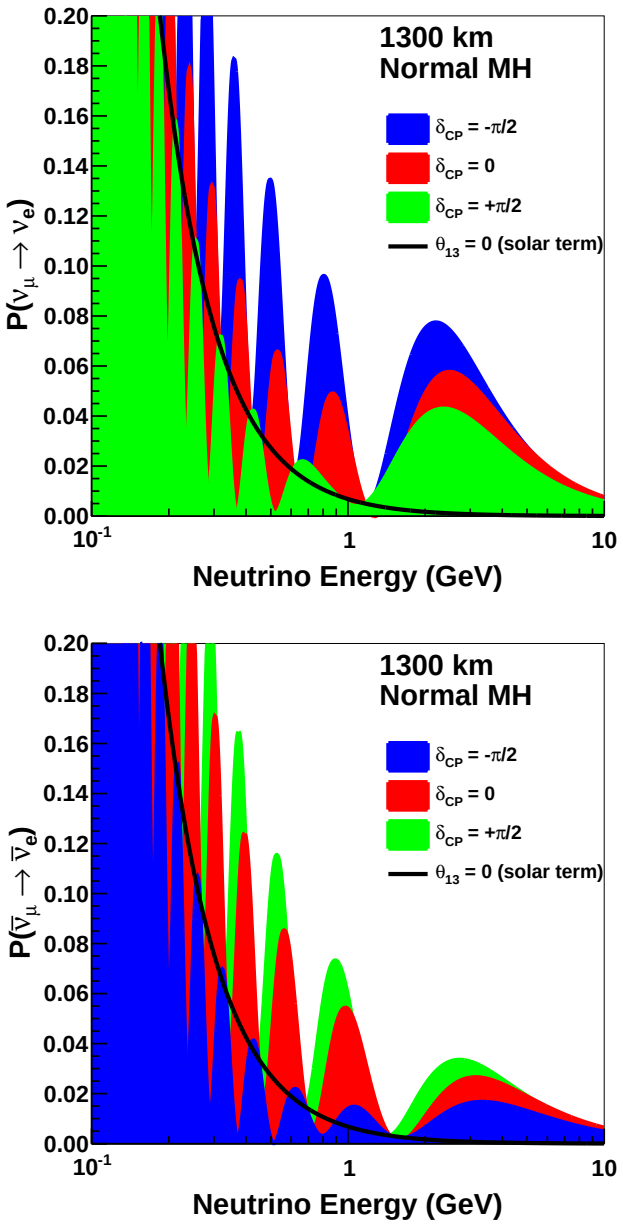

FIG. 1: The appearance probability at a baseline of 1300 km, as a function of neutrino energy, for $\delta_{\rm CP} = -\pi/2$ (blue), 0 (red), and $\pi/2$ (green), for neutrinos (top) and antineutrinos (bottom), for normal ordering. The black line indicates the oscillation probability if θ_{13} were equal to zero. Note that DUNE will be built at a baseline of 1285 km.

model may be performed.

This paper describes studies that quantify DUNE's expected sensitivity to long-baseline neutrino oscillation. The flux simulation and associated uncertainties are described in Section II. Section III describes the neutrino interaction model and sytematic variations. The near and far detector simulation, reconstruction, and event selections are described in Sections IV and V, respectively, with a nominal set of event rate predictions given in Section VI. Detector uncertainties are described in Section VII. The methods used to extract oscillation sensitivities are described in Section VIII. The primary sensitivity results are presented in Section IX. Section X describes studies of the impact of the near detector on the oscillation analysis. We present our conclusions in Section XI.

II. NEUTRINO BEAM FLUX AND UNCERTAINTIES

The expected neutrino flux is generated using G4LBNF, a GEANT4-based simulation of the LBNF neutrino beam. The simulation is configured to use a detailed description of the Long-Baseline Neutrino Facility (LBNF) optimized beam design [10], which includes horns and target designed to maximize sensitivity to CPV given the physical constraints on the beamline design.

Neutrino fluxes for neutrino and antineutrino mode configurations of LBNF are shown in Figure 2. Uncertainties on the neutrino fluxes arise primarily from uncertainties in hadrons produced off the target and uncertainties in the design parameters of the beamline, such as horn currents and horn and target positioning (commonly called "focusing uncertainties"). Given current measurements of hadron production and LBNF estimates of alignment tolerances, flux uncertainties are approximately 8% at the first oscillation maximum and 12% at the second. These uncertainties are highly correlated across energy bins and neutrino flavors.

The unoscillated fluxes at the near detector (ND) and FD are similar, but not identical (since the ND sees a line source, while the FD sees a point source. The relationship is well understood, and flux uncertainties mostly cancel for the ratio of fluxes between the two detectors. Uncertainties on the ratio are around 1% or smaller except at the falling edge of the focusing peak, where they rise to 2%. The far to near flux ratio and uncertainties on this ratio are shown in Fig. 3.

Uncertainties on the flux prediction are described by a covariance matrix, where each bin corresponds to an energy range of a particular beam mode, neutrino species, and detector location. The covariance matrix includes all beam focusing uncertainties evaluated by reproducing the simulation many times, each with simultaneous random variations in the underlying hadron production model. Each random model variation is referred to as a universe. The matrix used is 208 × 208 bins, despite having only ∼30 input uncertainties (and thus ∼30 significant eigenvalues). To evaluate the impact of these uncertainties on the long-baseline oscillation sensitivity, it is possible to include each focusing parameter, and each hadron production universe, as separate nuisance parameters. It is also possible to treat each bin of the prediction as a separate nuisance parameter, and include the covariance matrix in the log-likelihood calculation. However,

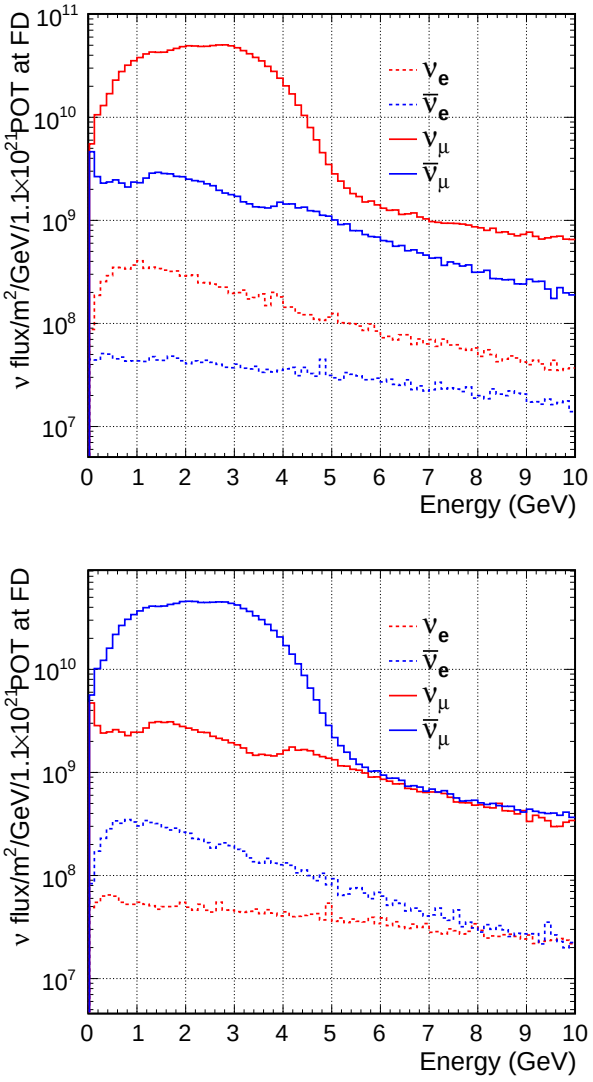

FIG. 2: Neutrino fluxes at the FD for neutrino mode (top) and antineutrino mode (bottom).

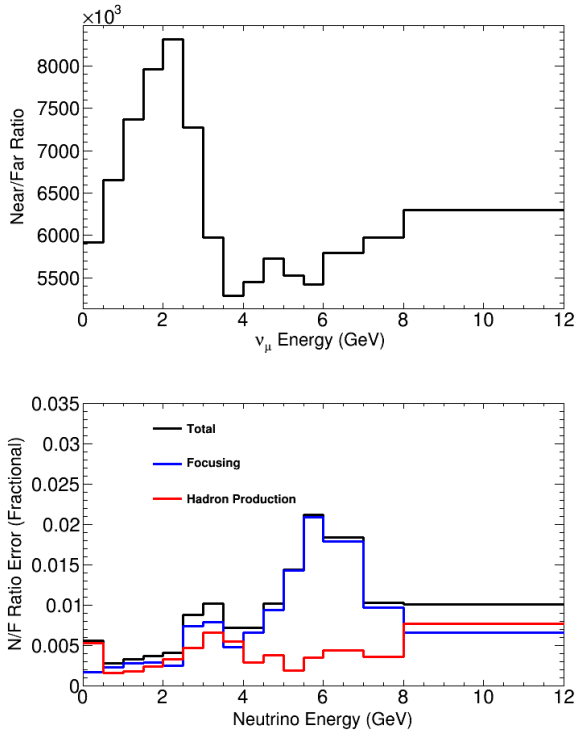

FIG. 3: Ratio of neutrino-mode muon neutrino fluxes at the near and far detectors (top) and uncertainties on the ratio (bottom). To be updated.

both of these options are computationally expensive, and would include many nuisance parameters with essentially no impact on any distributions.

Instead, the covariance matrix is diagonalized, and each principal component is treated as an uncorrelated nuisance parameter. The 208 principal components are ordered by the magnitude of their corresponding eigenvalues, and only the first ∼30 are large enough that they need to be included. By the 10th principal component, the eigenvalue is 1% of the 0th eigenvalue. Since the time required to perform a fit scales ∼linearly with the number of nuisance parameters, including only 30 principal components reduces the computing time by an order of magnitude.

This is purely a mathematical transformation; the same effects are described by the PCA as by a full analysis, including correlations between energy bins. As expected, the largest uncertainties correspond to the largest principal components. This can be seen in Figure 4. The largest principal component matches the hadron production uncertainty on nucleon-nucleus interactions in a phase space region not covered by data (N+A unconstrained). Components 3 and 7 correspond to the data-constrained uncertainty on proton interactions in the target producing pions and kaons, respectively. Components 5 and 11 correspond to two of the largest focusing uncertainties, the density of the target and the horn current, respectively. Other components not shown either do not fit a single uncertain parameter and may represent two or more degenerate systematics or ones that produce anticorrelations in neighboring energy bins.

CW: I wonder whether we should add in the following paragraph about assumed hadron production uncertainties? Future hadron production measurements are expected to improve the quality of and the resulting constraints on these flux uncertainty estimates. Approximately 40% of the interactions that produce neutrinos in the LBNF beam simulation have no data constraints whatsoever. Large uncertainties are assumed for these interactions. The largest unconstrained sources of uncertainty are proton quasielastic interactions and meson incident interactions. The proposed EMPHATIC experiment [CITATION NEEDED] at Fermilab will be able to constrain quasielastics and low energy interactions that

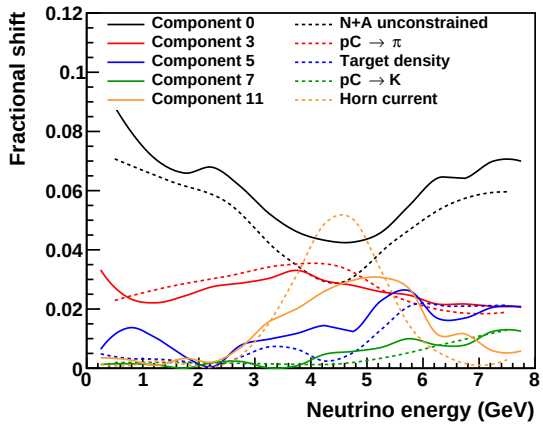

FIG. 4: Select flux principal components are compared to specific underlying uncertainties from the hadron production and beam focusing models.

Description of P	P_{cv}
Quasielastic	
Random Phase Approximation tune	A : 0.59
A controls low Q^2, B controls low-mid Q^2	B : 1.05
D controls mid Q^2, E controls high Q^2 fall-off	D : 1.13
U controls transition from polynomial to exponential	E : 0.88
	U : 1.20
2p2h	
$q0, q3$ dependent correction to 2p2h events	
Low W single pion production	
Axial mass for CC resonance in GENIE	0.94
Normalization of CC1π non-resonant interaction	0.43

TABLE I: Neutrino interaction cross-section systematic parameters that receive a central-value tune.

dominate the lowest neutrino energy bins. The NA61 experiment at CERN has taken data that will constrain many higher energy interactions, including meson incident, and also plans to measure hadrons produced off of a replica LBNF target, which would provide tight constraints on all interactions occurring in the target. A similar program at NA61 has reduced flux uncertainties for T2K from 10% to 5% [11], and NOvA is currently analyzing NA61 replica target data [12]. Another proposed experiment, the LBNF spectrometer, would measure hadrons after both production and focusing in the horns, effectively constraining nearly all hadron production uncertainties, and could also enable measurement of the impact on focused hadrons of shifted alignment parameters (which is currently taken from simulations).

III. NEUTRINO INTERACTIONS AND UNCERTAINTIES

A framework for considering the impact of neutrino interaction model uncertainties on the oscillation analysis has been developed. This model generally, though not in all cases, factorizes the neutrino interaction on nuclei into an incoherent sum of hard scattering neutrino interactions with the single nucleons in the nucleus. The effect of the nucleus is implemented as initial and final state interaction effects, with some nucleus-dependent hard scattering calculations.

The initial state effects relate to the description of the momentum and position distributions of the nucleons in the nucleus, kinematic modifications to the final state (such as separation energy, sometimes described as a binding energy), and Coulomb effects. The concept of binding energy reflects the idea that the struck nucleon may be off the mass-shell inside the nucleus. final-state interactions (FSI) refer to the propagation and interaction of hadrons produced in the nucleon interaction through the nucleus. The FSI alter both the momentum and energy of the recoiling particles produced in the final state, and may also alter their identity and multiplicity in the case of inelastic reinteractions (e.g., in a nucleus a hadron may be absorbed, rescattered, or create a secondary hadron). The FSI model implemented in the GENIE, NuWro, and NEUT neutrino interaction generators is a semi-classical cascade model. In the specific case of GENIE's hA model a single step scaled model, based on hadron-nucleus and hadron-nucleon scattering data and theoretical corrections.

The default interaction model is implemented in v2.12.10 of the GENIE generator. There are a number of tunes applied to the default model, to represent known deficiencies in GENIE's description of neutrino data; these are listed in Table I. Variations in the cross sections to be considered are implemented as some combination of GENIE weighting parameters (sometimes referred to as "GENIE knobs"), *ad hoc* weights of events that are designed to parameterize uncertainties or cross section corrections currently not implemented within GENIE, and discrete alternative model comparisons, achieved through alternative generators, alternative GENIE configurations, or custom weightings.

The interaction uncertainties are divided into seven roughly exclusive groups: (1) initial state uncertainties, (2) hard scattering uncertainties and nuclear modifications to the quasielastic process, (3) uncertainties in multinucleon (2p2h) hard scattering processes, (4) hard scattering uncertainties in pion production processes, (5) uncertainties governing other, higher W and neutral current processes, (6) final state interaction uncertainties, (7) neutrino flavor dependent uncertainties. Uncertainties are intended to reflect current theoretical freedom,

deficiencies in implementation, and/or current experimental knowledge. There are some constraints on nuclear effects because of measurements on lighter targets; however, for the argon nuclear target some additional sources of uncertainty are identified.

The default nuclear model in GENIE is a modified global Fermi gas model of the nucleons in the nucleus. There are significant deficiencies that are known in global Fermi gas models; these include a lack of consistent incorporation of the tails that result from correlations among nucleons, the lack of correlation between location within the nucleus and momentum of the nucleon, an incorrect relationship between momentum and energy of the off-shell, bound nucleon within the nucleus. GENIE modifies the nucleon momentum distribution empirically to account for short-range correlation effects, which populates tails above the Fermi cutoff, but the other deficiencies persist. Alternative initial state models, such as spectral functions [13, 14], the mean field model of GiBUU [15], or continuum random phase approximation (CRPA) calculations [16] may provide better descriptions of the nuclear initial state [17].

An important Fermi gas parameter which enters directly into neutrino energy reconstruction is the binding or removal energy, E_B. This parameter directly affects the transfer of energy to the nucleus. It cannot be implemented by event weights within the GENIE Fermi gas model, and is implemented by a "lateral" shift of lepton energies as a function of neutrino energy and lepton energy, following T2K's implementation. For GENIE, the recommendation from Ref. [18] is to set E_b to 17.8 ± 3 MeV in neutrino interactions and 21.8 ± 3 MeV in antineutrino interactions. Note that these values significant differ from the GENIE default.

The primary uncertainties considered in quasielastic interactions are the axial form factor of the nucleon and nuclear screening—from the so-called Random Phase Approximation (random phase approximation (RPA)) calculations—of low momentum transfer reactions.

One part of the Nieves et al.[19, 20] description of the 0π interaction on nuclei includes RPA, used to sum the $W^{\pm}$ self-energy terms. In practice, this modifies the 1p1h/Quasi-Elastic cross-section in a non-trivial way. The calculations from Nieves et al. have associated uncertainties presented in [21], which were evaluated as a function of Q^2 [22]. In 2018, MINERvA and NOvA parameterized the central value and uncertainty in (q_0, q_3) using RPA uncertainties as parameterized in [23], whereas T2K used central values and uncertainties in Q^2 only. Here we use T2K's 2017/8 parameterization of the RPA effect[24] due to its simplicity. The shape of the correction and error is parameterized with a Bernstein polynomial up to $Q^2 = 1.2$ GeV^2 which switches to a decaying exponential. The BeRPA (Bernstein RPA) function has three parameters controlling the polynomial (A, B, C), where the parameters control the behavior at increasing Q^2 and a fourth parameter E controls the high Q^2 tail. The axial form factor parameterization we use is known to be inadequate. However, the convolution of BeRPA uncertainties with the limited axial form factor uncertainties do provide more freedom as a function of Q^2, and the two effects likely provide adequate freedom for the Q^2 shape in quasielastic events.

We start with the Nieves et al. or "Valencia" model [19, 20] for multinucleon ($2p2h$) contributions to the cross section. However, MINERvA has shown directly [25], and NOvA indirectly, that this description is missing observed strength on carbon. As a primary approach to the model, we add that missing strength to a number of possible reactions. We then add uncertainties for energy dependence of this missing strength and uncertainties in scaling the $2p2h$ prediction from carbon to argon.

The extra strength from the "MINERvA tune" to $2p2h$ is applied in (q_0, q_3) space (where q_0 is energy transfer from the leptonic system, and q_3 is the magnitude of the three momentum transfer) to fit reconstructed MINERvA CC-inclusive data [25] in E_{avail}[55] and q_3. Reasonable fits to MINERvA's data are found by attributing the missing strength to any of $2p2h$ from np initial state pairs, $2p2h$ from nn initial state pairs, or $1p1h$ or quasielastic processes. The default tune uses an enhancement of the np and nn initial strengths in the ratio predicted by the Nieves model, and alternative systematic variation tunes ("MnvTune" 1-3) attribute the missing strength to the individual hypotheses above. Implementation of the "MnvTune" is based on weighting in true (q_0, q_3). The weighting requires GENIE's Llewelyn-Smith $1p1h$ and Valencia $2p2h$ are used as the base model. To ensure consistency in using these different tunes as freedom in the model, a single systematic parameter is introduced that varies smoothly between applying the $1p1h$ tune at one extreme value to applying the nn tune at the other extreme via the default tune which is used as the central value. The np tune is neglected in this prescription as being the most redundant, in terms of missing energy content of the final state, of the four discrete hypotheses.

The rates for $1p1h$ and $2p2h$ processes could be different on argon and carbon targets. There is little neutrino scattering data to inform this, but there are measurements of short-ranged correlated pairs from electron scattering on different nuclei [26]. These measurements directly constrain $2p2h$ from short range correlations, although the link to dynamical sources like meson exchange current processes (MEC) is less direct. Interpolation of that data in A (Nucleon number) suggests that scaling from carbon relative to the naive $\propto A$ prediction for $2p2h$ processes would give an additional factor of 1.33 ± 0.13 for np pairs, and 0.9 ± 0.4 for pp pairs. GENIE's prediction for the ratio of $2p2h$ cross-sections in $\text{Ar}^{40}/\text{C}^{12}$ for neutrinos varies slowly with neutrino energy in the DUNE energy range: from 3.76 at 1 GeV to 3.64 at 5 GeV. The ratio for antineutrino cross sections is consistent with 3.20 at all DUNE energies. Since the ratio of A for $\text{Ar}^{40}/\text{C}^{12}$ is 3.33, this is consistent with the ranges suggested above by the measured pp and np pair scaling.

A dedicated study by the SuSA group using their own theoretical model for the relevant MEC process also concludes that the transverse nuclear response (which drives the $\nu - A$ MEC cross section) ratio between Ca^{40} (the isoscalar nucleus with the same A as Ar^{40}) and C^{12} is 3.72 [27]. We vary GENIE's Valencia model based prediction, including the MINERvA tune, for $2p2h$ by $\sim 20\%$ to be consistent with the correlated pair scaling values above. This is done independently for neutrino and antineutrino scattering.

The MINERvA tune may be E_ν dependent. MINERvA separated its data into an $E_\nu < 6$ GeV and an $E_\nu >6$ GeV piece, and sees no dependence with a precision of better than 10% [25]. The mean energy of the $E_\nu < 6$ GeV piece is roughly $\langle E_\nu \rangle \approx 3$ GeV. In general, an exclusive cross-section will have an energy dependence $\propto \frac{A}{E_\nu^2} + \frac{B}{E_\nu} + C$ [28]; therefore, unknown energy dependence may be parametrized by an *ad hoc* factor of the form $1/\left(1 + \frac{A^{'}}{E_\nu^2} + \frac{B^{'}}{E_\nu}\right)$. The MINERvA constraints suggest $A^{'} < 0.9$ GeV^2 and $B^{'} < 0.3$ GeV. The variations for neutrinos and antineutrinos could be different since this is an effective modification. Ideally this energy dependent factor would only affect the MINERvA tune, but practically, because of analysis framework limitations already discussed, this is not possible. As a result, this energy dependent factor is applied to all true $2p2h$ events.

GENIE uses the Rein-Sehgal model for pion production. Tunes to D_2 data have been performed, both by the GENIE collaboration itself and in subsequent re-evaluations [29, 30]; we use the latter tune as our base model. For simplicity of implementation, the 'v2.8.2 (no norm.)' results are used here.

Coherent inelastic pion production measurements on carbon are in reasonable agreement with the GENIE implementation of the Berger-Sehgal model [31]. The process has not been measured at high statistics in argon. While coherent interactions provide a very interesting sample for oscillation analyses, they are a very small component of the event rate and selections will depend on the near detector configuration. Therefore we do not provide any evaluation of a systematic uncertainty for this extrapolation or any disagreements between the Berger-Sehgal model and carbon data.

NOvA oscillation analyses [32] have found the need for excursions beyond the default GENIE uncertainties to describe their single pion to deep inelastic scattering (DIS) transition region data. Following suit, we drop GENIE's default "Rv[n,p][1,2]pi" knobs and instead implement separate, uncorrelated uncertainties for all perturbations of 1, 2, and $\geq$ 3 pion final states, CC/NC, neutrinos/anti-neutrinos, and interactions on protons/neutrons, with the exception of CC neutrino 1-pion production, where interactions on protons and neutrons are merged, following [30]. This leads to 23 distinct uncertainty channels ([3 pion states] x [n,p] x [nu/anti-nu] x [CC/NC] - 1), all with a value of 50% for $W \leq 3$ GeV. For each channel, the uncertainty drops linearly above $W = 3$ GeV until it reaches a flat value of 5% at $W = 5$ GeV, where external measurements better constrain this process.

GENIE includes a large number of final state uncertainties to its hA final state cascade model which are summarized in Table III. These uncertainties have been validated in neutrino interactions primarily on light targets such as carbon, but there is very little data available on argon targets.

The cross sections include terms proportional to lepton mass, which are significant contributors at low energies where quasielastic processes dominate. Some of the form factors in these terms have significant uncertainties in the nuclear environment. Ref. [33] ascribes the largest possible effect to the presence of poorly constrained second-class current vector form factors in the nuclear environment, and proposes a variation in the cross section ratio of σ_μ/σ_e of $\pm 0.01/\text{Max}(0.2\text{ GeV}, E_\nu)$ for neutrinos and $\mp 0.018/\text{Max}(0.2\text{ GeV}, E_\nu)$ for anti-neutrinos. Note the anticorrelation of the effect in neutrinos and antineutrinos.

Finally, some electron neutrino interactions occur at four momentum transfers where a corresponding muon neutrino interaction is kinematically forbidden, therefore the nuclear response has not been constrained by muon neutrino cross section measurements. This region at lower neutrino energies has a significant overlap with the Bodek-Ritchie tail of the Fermi gas model. There are significant uncertainties in this region, both from the form of the tail itself, and from the lack of knowledge about the effect of RPA and $2p2h$ in this region. The allowed phase space in the presence of non-zero lepton mass is $E_\nu - \sqrt{(E_\nu - q_0)^2 - m_l^2} \leq q_3 \leq E_\nu + \sqrt{(E_\nu - q_0)^2 - m_l^2}$. Here, a 100% variation is allowed in the phase space present for ν_e but absent for ν_μ.

The complete set of interaction model uncertainties includes GENIE implemented uncertainties (Tables II, and III), and new uncertainties developed for this effort (Table IV) which represent uncertainties beyond those implemented in the GENIE generator.

The way model parameters are treated in the analysis is described by three categories:

- Category 1: On-axis near detector data is expected to constrain these parameters; the uncertainty is implemented in the same way in near and far detectors.

- Category 2: These uncertainties are implemented in the same way in near and far detectors, but on-axis data alone is not sufficient to constrain these parameters. The first sub-category (2A) corresponds to interaction effects which may be difficult to disentangle from detector effects. The second sub-category (2B) corresponds to parameters that can be constrained by off-axis samples, described in Section IV.

- Category 3: These uncertainties are implemented

Description of P	$\delta P/P$
Quasielastic	
Axial mass for CCQE	$^{+0.25}_{-0.15}$ GeV
Choice of CCQE vector form factors (BBBA05 $\leftrightarrow$ Dipole)	N/A
Fermi surface momentum for Pauli blocking	±30%
Low W	
Axial mass for CC resonance	±0.05 GeV
Vector mass for CC resonance	±10%
Branching ratio for $\Delta \rightarrow \eta$ decay	±50%
Branching ratio for $\Delta \rightarrow \gamma$ decay	±50%
θ_π distribution in decaying Δ rest frame (isotropic $\rightarrow$ RS)	N/A
High W	
A_{HT} higher-twist param in BY model scaling variable ξ_w	±25%
B_{HT} higher-twist param in BY model scaling variable ξ_w	±25%
C_{V1u} valence GRV98 PDF correction param in BY model	±30%
C_{V2u} valence GRV98 PDF correction param in BY model	±40%
Other neutral current	
Axial mass for NC elastic	±25%
Strange axial form factor η for NC elastic	±30%
Axial mass for NC resonance	±10%
Vector mass for NC resonance	±5%
Misc.	
Vary effective formation zone length	±50%

TABLE II: Neutrino interaction cross-section systematic parameters considered in GENIE. GENIE default central values and uncertainties are used for all parameters except $x_{M_A}^{CCRES}$. Missing GENIE parameters were omitted where uncertainties developed for this analysis significantly overlap with the supplied GENIE freedom, the response calculation was too slow, or the variations were deemed unphysical.

Description of P	$\delta P/P$
Nucleon charge exchange probability	±50%
Nucleon elastic reaction probability	±30%
Nucleon inelastic reaction probability	±40%
Nucleon absorption probability	±20%
Nucleon π-production probability	±20%
π charge exchange probability	±50%
π elastic reaction probability	±10%
π inelastic reaction probability	±40%
π absorption probability	±20%
π π-production probability	±20%

TABLE III: The intra-nuclear hadron transport systematic parameters implemented in GENIE with associated uncertainties considered in this work. Note that the 'mean free path' parameters are omitted for both N-N and π-N interactions as they produced unphysical variations in observable analysis variables. Table adapted from Ref [34].

only in the far detector. Examples are ν_e and $\overline{\nu}_e$ rates which are small and difficult to precisely isolate from background at the near detector. Therefore, near detector data is not expected to constrain such parameters.

GENIE uncertainties (original or modified) are all treated as Category 1. Table IV, which describes the uncertainties beyond those available within GENIE, includes a column identifying which of these categories describes the treatment of each additional uncertainty.

IV. THE NEAR DETECTOR SIMULATION AND RECONSTRUCTION

The baseline design for the DUNE ND system consists of a liquid argon time-projection chamber (LArTPC) functionally coupled to a magnetized multi-purpose detector (MPD), and a 3D scintillator tracker (3DST). The ND hall is located at Fermi National Accelerator Laboratory (Fermilab) 574 m from the neutrino beam source and 60 m underground. The long dimension of the hall is oriented at 90 degrees with respect to the beam axis to facilitate measurements at both on-axis and off-axis locations with a movable detector system. The use of off-axis angles is complementary to the on-axis analysis described in this work, and further details can be found in Ref. [CITATION NEEDED] . The 3DST will primarily function as a beam monitor, as described in Ref. [CITATION NEEDED] . Although 3DST and off-axis samples are not used explicitly in this analysis, there is an implicit assumption that they will be in place to control systematic uncertainties to the level considered here.

The LArTPC is modular, with fully-3D pixelated readout and optical segmentation. These features greatly reduce reconstruction ambiguities that hamper monolithic, projective-readout time projection chambers (TPCs), and enable the ND to function in the high-intensity environment of the DUNE ND site. Each module is itself a liquid argon (LAr) TPC with two anode planes and a central cathode. The active dimensions of each module are $1 \times 3 \times 1$ m ($x \times y \times z$), where the z direction is 6° upward from the neutrino beam, and the y direction

Uncertainty	Mode	Description	Category
BeRPA	1p1h/QE	RPA/nuclear model suppression	1
MnvTune1	2p2h	Strength into (nn)pp only	1
MnvTuneCV	2p2h	Strength into 2p2h	1
MnvTune2	1p1h/QE	Strength into 1p1h	1
ArC2p2h	2p2h Ar/C scaling	Electron scattering SRC pairs	1
E_{2p2h}	2p2h	2p2h Energy dependence	2B
Low Q^2 1π	RES	Low Q^2 (empirical) suppression	1
MK model	ν_μ CC-RES	alternative strength in W	1
CC Non-resonant $\nu \to \ell + 1\pi$	ν DIS	Norm. for $\nu + n/p \to \ell + 1\pi$ (*c.f.[30]*)	1
Other Non-resonant π	$N\pi$ DIS	Per-topology norm. for $1 < W < 5$ GeV.	1
E_{avail}/q_0	all	Extreme FSI-like variations	2B
Modified proton energy	all	20% change to proton E	2B
$\nu_\mu \to \nu_e$	$\nu_e/\overline{\nu}_e$	100% uncertainty in ν_e unique phase space	3
$\nu_e/\overline{\nu}_e$ norm	ν_e,$\overline{\nu}_e$	Ref. [33]	3

TABLE IV: List of extra interaction model uncertainties in addition to those provided by GENIE.

points upward. Charge drifts in the $\pm x$ direction, with a maximum drift distance of 50 cm for ionization electrons produced in the center of a module. The module design is described in detail in Ref. [35] CW: is this actually the correct reference???. The full LAr detector consists of an array of modules in a single cryostat. The minimum active size for full containment of hadronic showers is $3 \times 4 \times 5$ m. High-angle muons can also be contained by extending the width to 7 m. For this analysis, 35 modules are arranged in an array 5 modules deep in the z direction and 7 modules across in x so that the total active dimensions are $7 \times 3 \times 5$ m. The total active LAr volume is 105 m^3, corresponding to a mass of 147 tons.

The MPD consists of a high-pressure gaseous argon time-projection chamber (GArTPC) in a cylindrical pressure vessel at 10 bar, surrounded by a granular, high-performance electromagnetic calorimeter. The MPD sits immediately downstream of the LAr cryostat so that the beam center crosses the exact center of both the LAr and gaseous argon active volumes. The pressure vessel is 5 m in diameter and 5 m long. The TPC is divided into two drift regions by a central cathode, and filled with a 90/10 Ar/CH_4 gas mixture, such that 97% of neutrino interactions will occur on the Ar target. The gas TPC is described in detail in Ref. [36]. The electromagnetic calorimeter is composed of a series of absorber layers followed by arrays of scintillator. The electromagnetic calorimeter (ECAL) design is described in Ref. [37]. The entire MPD sits inside a magnetic field with a strength of at least 0.4 T.

A. Event Simulation and Parameterized Reconstruction

Neutrino interactions are simulated in the active volumes of the LAr and high-pressure gas (HPG) TPCs. The neutrino flux prediction is described in Section II. Interactions are simulated with the GENIE event generator using the model configuration described in Section III. The propagation of neutrino interaction products through the detector volumes is simulated using a Geant4-based model. Pattern recognition and reconstruction software has not yet been developed for the ND. Instead, we perform a parameterized reconstruction based on true energy deposits in active detector volumes as simulated by Geant4.

Liquid argon events are required to originate in a fiducial volume that excludes 50 cm from the sides and upstream edge, and 150 cm from the downstream edge of the active region, for a total of $6 \times 2 \times 3$ m^2. A hadronic veto region is defined as the outer 30 cm of the active volume on all sides. Events with more than 30 MeV total energy deposit in the veto region are excluded from analysis, as this energy near the detector edge suggests leakage, resulting in poor energy reconstruction. Even with the containment requirement, events with large shower fluctuations to neutral particles can still be very poorly reconstructed. Neutrons, in particular, are largely unreconstructed energy.

Electrons are reconstructed calorimetrically in the liquid argon. The radiation length is 14 cm in LAr, so for fiducial interactions and forward-going electrons there are between 10 and 30 radiation lengths between the ver-

tex and the edge of the TPC. As there is no magnetic field in the LAr TPC region, electrons and positrons cannot be distinguished and the selected ν_e sample contains both neutrino- and antineutrino-induced events.

Muons with kinetic energy greater than ∼1 GeV typically exit the LAr. An energetic forward-going muon will pass through the ECal and into the gaseous TPC, where its momentum and charge are reconstructed by curvature. For these events, it is possible to differentiate between μ^+ and μ^- event by event. Muons that stop in the LAr or ECal are reconstructed by range. Exiting muons that do not match to the HPG TPC are not reconstructed, and events with these tracks are rejected from analysis. These are predominantly muon charged current (CC), where the muon momentum cannot be determined. Forward exiting muons will enter the magnetized MPD, where their momenta and charge sign are reconstructed by curvature. The asymmetric transverse dimensions of the LAr volume make it possible to reconstruct wide-angle muons with some efficiency. High-angle tracks are typically lost when the $\nu-\mu$ plane is nearly parallel to the y axis, but are often contained when it is nearly parallel to the x axis.

The charge of stopping muons in the LAr volume cannot be determined. However, the wrong-sign flux is predominantly concentrated in the high-energy tail, where leptons are likelier to be forward and energetic. In FHC mode, the wrong-sign background in the focusing peak is negligibly small, and μ^- is assumed for all stopping muon tracks. In RHC mode, the wrong-sign background is larger in the peak region. Furthermore, high-angle leptons are generally at higher inelasticity, y, which enhances the wrong-sign contamination in the contained muon subsample. To mitigate this, a Michel electron is required. The wrong-sign μ^- captures on Ar with 75% probability, effectively suppressing the relative μ^- component by a factor of four.

Events are classified as either ν_μ CC, $\bar{\nu}_\mu$ CC, $\nu_e+\bar{\nu}_e$ CC, or NC. True muons and charged pions are evaluated as potential muon candidates. The track length is determined by following the true particle trajectory until it hard scatters or ranges out. The particle is classified as a muon if its track length is at least 1 m, and the mean energy deposit per centimeter of track length is less than 3 MeV. The mean energy cut rejects tracks with detectable hadronic interactions. The minimum length requirement imposes an effective threshold on true muons of about 200 MeV kinetic energy, but greatly suppresses potential NC backgrounds with short, non-interacting charged pions.

True electrons are reconstructed with an ad-hoc efficiency that is zero below 300 MeV, and rises linearly to unity between 300 and 700 MeV. Neutral-current backgrounds arise from photon and π^0 production. Photons are misreconstructed as electrons when the energy deposit per centimeter in the first few cm after conversion is less than 4 MeV. This is typically for Compton scatters, and can also occur due to a random downward fluctuation in the e^+e^- dE/dx. The conversion distance must also be small so that no visible gap can be identified. We consider a photon gap to be clear when the conversion distance is greater than 2 cm, which corresponds to at least four pad widths. For π^0 events, the second photon must also be either less than 50 MeV, or have an opening angle to the first photon less than 10 mrad. Electrons are generally contained in the LAr and are reconstructed calorimetrically. It is possible for CC ν_μ events to be reconstructed as CC ν_e when the muon is too soft and a π^0 fakes the electron.

Charged-current events are required to have exactly one reconstructed lepton of the appropriate flavor. The muon-flavor samples are separated by reconstructed charge, but the electron-flavor sample is combined because the charge cannot be determined. The neutral-current sample includes all events with zero reconstructed leptons. Spectra for selected ν_μ CC events in FHC are shown in Figure 5 as a function of both neutrino energy and inelasticity.

Hadronic energy is estimated by summing visible energy deposits in the active LAr volume. Events are rejected when energy is observed in the outer 30 cm of the detector, which is evidence of poor hadronic containment. Events with more than 30 MeV of visible hadronic energy in the veto region are also excluded. This leads to an acceptance that decreases with hadronic energy, as shown in the right panel of Figure 6.

Backgrounds to ν_μ CC arise from neutral current (NC) $\pi^\pm$ production where the pion leaves a long track and does not shower. Muons below about 400 MeV kinetic energy have a significant background from charged pions, so these CC events are excluded from the selected sample. Backgrounds to ν_e CC arise from photons that convert very near the interaction vertex. The largest contribution is from π^0 production with highly asymmetric decay.

B. ND samples in oscillation analysis

The oscillation analysis presented here includes samples of ν_μ and $\bar{\nu}_\mu$ charged-current interactions originating in the LAr portion of the ND. These samples are binned in two-dimensions as a function of reconstructed neutrino energy and inelasticity, $y = 1 - E_\mu/E_\nu$, where E_μ and E_ν are the reconstructed muon and neutrino energies, respectively. While not explicitly included in the analysis presented here, the assumptions regarding near detector performance and the associated constraints on systematic uncertainty require measurements from the full near detector suite.

We note that there are many samples not included in the current analysis.

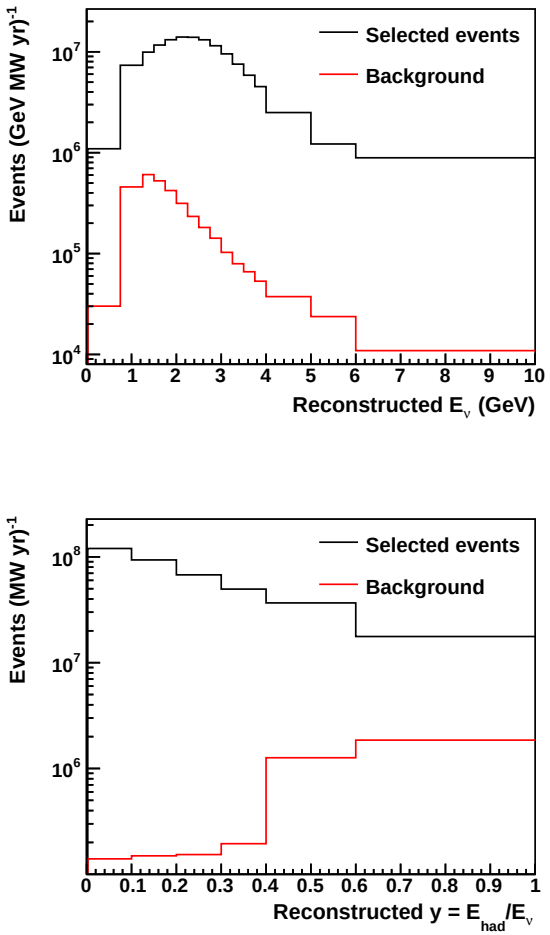

FIG. 5: Reconstructed neutrino energy (top) and y (bottom) for events classified as ν_μ CC in FHC mode. Background events are predominantly neutral currents and are shown in red.

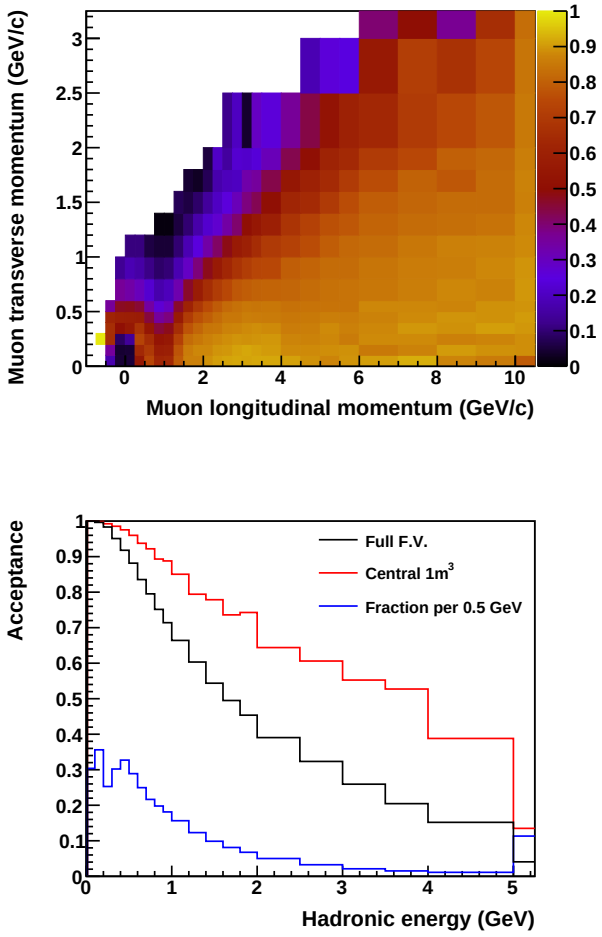

FIG. 6: Top: Detector acceptance for ν_μ CC events as a function of muon transverse and longitudinal momentum. Bottom: Acceptance as a function of hadronic energy; the black line is for the full fiducial volume while the red line is for a $1 \times 1 \times 1$ m^3 volume in the center, and the blue curve is the expected distribution of hadronic energy given the DUNE flux.

V. THE FAR DETECTOR SIMULATION AND RECONSTRUCTION

The calculation of DUNE sensitivities to oscillation parameter measurements requires predictions for the number of events to be observed in the FD fiducial volume, the reconstructed neutrino energy for each of these events, and the probability that they will be correctly identified as signal for each analysis samples. To build these analysis samples a Geant4 simulation of the FD has been developed. The output of that simulation has been used to build neutrino energy estimators, and an event selection discriminant that can separate ν_e CC, ν_μ CC, and NC events. Each of these components is described in detail in this section. The uncertainties associated with each step in the simulation and reconstruction chain, including the FD simulation, reconstructed energy estimators, and selection efficiencies are discussed in Section VII.

A. Simulation

The neutrino samples were simulated using a smaller version of the full 10 kt far detector module geometry. This geometry is 13.9 m long, 12.0 m high and 13.3 m wide, which consists of 12 anode plane assemblies (APAs) and 24 cathode plane assemblies (CPAs). The reference flux was used (Section II) and samples were produced with both the forward-horn-current (neutrino enhanced) and inverted-horn-current (antineutrino enhanced) beam configurations. Three samples were generated. The first sample keeps the original neutrino flavor composition of the neutrino beam. The second sample converts all the

muon neutrinos to electron neutrinos. The third sample converts all the muon neutrinos to tau neutrinos. Oscillation probabilities are used to weight CC events to build oscillated FD predictions from the three event samples. The nominal interaction model described in Section III was used to model the neutrino-argon interactions in the volume of cryostat. The produced final-state (after FSI) particles were propagated in the detector through Geant4. The ionization electrons and scintillation light were digitized to produce signals in the wire planes and photon detectors (PDs).

B. Event Reconstruction and Kinematic Variables

Raw detector signals are processed using algorithms to remove the impact of the LArTPC electric field and electronics response from the measured signal, to identify "hits," and to performing "clustering" on hits that may be grouped together due to proximity in time and space to one another. Clusters from different wire planes are matched to form high-level objects such as tracks and showers. These high level objects are used as inputs to the neutrino energy reconstruction algorithm.

The energy of the incoming neutrino in CC events is estimated by adding the reconstructed lepton and hadronic energies. If the event is selected as ν_μ CC, the neutrino energy is estimated as the sum of the energy of the longest reconstructed track and the hadronic energy. The energy of the longest reconstructed track is estimated from its range if the track is contained in the detector, and this is calibrated using simulated ν_μ CC events with true muon energies from 0.2-1.7 GeV. If the longest track exits the detector, its energy is estimated from multi-Coulomb scattering, and corrected using simulated events with true muon energies from 0.5-3 GeV. The hadronic energy is estimated from the charge of reconstructed hits that are not in the longest track, and corrections are applied to each hit charge for recombination and the electron lifetime. An additional correction is then made to the hadronic energy to account for missing energy due to neutral particles and final-state interactions, and this is done using simulated events with true hadronic energies from 0.1-1.6 GeV. The same hadronic shower energy calibration is used for both ν and $\bar{\nu}$ based on a sample of ν and $\bar{\nu}$ events.

If the event is selected as ν_e CC, the energy of the neutrino is estimated as the sum of the energy of the reconstructed shower with the highest energy and the hadronic energy. The former is estimated from the charges of the reconstructed hits in the shower, and the latter from the hits not in the shower; the recombination and electron lifetime corrections are applied to the charge of each hit. Subsequently the shower energy is corrected using simulated events with true electron energies from 0.5-3 GeV, and the missing energy correction is applied to the hadronic energy.

The fractional residuals of reconstructed neutrino energy are shown for ν_μ CC events with contained tracks, ν_μ CC events with exiting tracks, and for ν_e CC events in figure 7. The biases and resolutions of reconstructed neutrino energy are summarized in Table V.

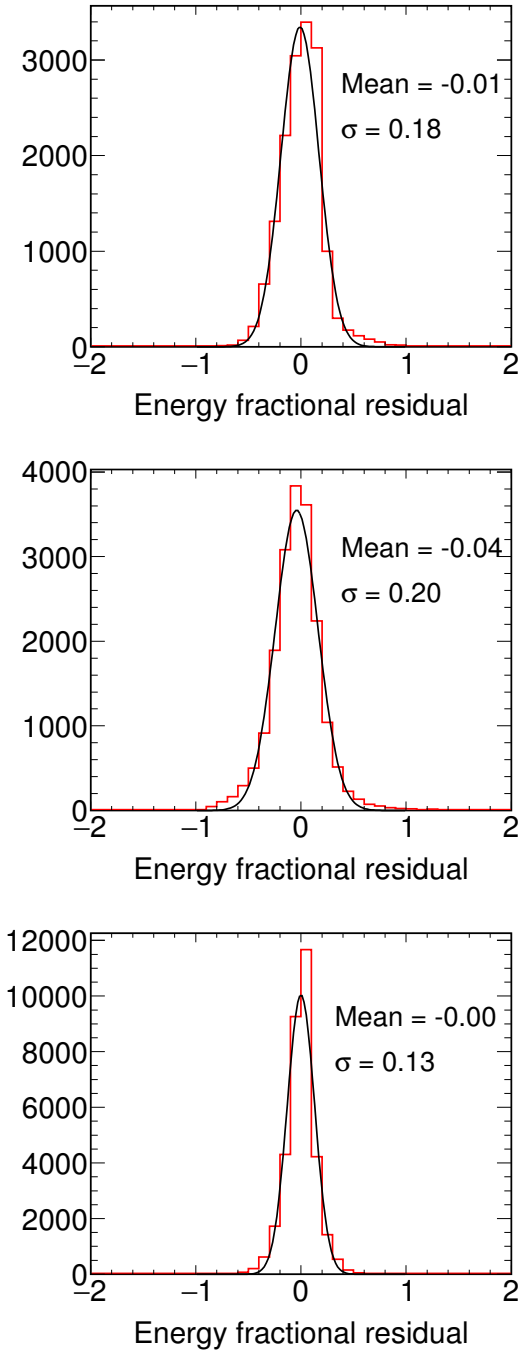

FIG. 7: Top: Fractional residuals of reconstructed ν_μ energy in ν_μ CC events with contained tracks; middle: Fractional residuals of reconstructed ν_μ energy in ν_μ CC events with exiting tracks; bottom: Fractional residuals of reconstructed ν_e energy in ν_e CC events.

Event selection	Bias (%)	Resolution (%)
ν_μ CC with contained track	-1	18
ν_μ CC with exiting track	-4	20
ν_e CC	0	13

TABLE V: Summary of biases and resolutions of reconstructed neutrino energy

FIG. 8: A simulated 2.2 GeV ν_e CC interaction shown in the collection view of the DUNE LArTPCs. The horizontal axis shows the wire number of the readout plane and the vertical axis shows time. The grayscale shows the charge of the energy deposits on the wires. The interaction looks similar in the other two views.

C. Neutrino Event Selection using convolutional visual network (CVN)

The DUNE CVN classifies neutrino interactions in the DUNE FD through image recognition techniques. In general terms it is a Convolutional Neural Network (CNN). Similar techniques have been demonstrated to outperform traditional methods in many aspects of high energy physics [38].

The primary goal of the CVN is to efficiently and accurately produce event selections of the following interactions: ν_μ CC and ν_e CC in the FHC beam mode, and $\bar{\nu}_\mu$ CC and $\bar{\nu}_e$ CC in the RHC beam mode. Detailed descriptions of the CVN architecture can be found in [39].

An important feature for the DUNE CVN is the fine-grained detail of a LArTPC encoded in the input images. To handle the level of detail, the CVN design is based on the SE-ResNet architecture, which consists of a standard ResNet (Residual neural network) architecture [40] along with Squeeze-and-Excitation blocks [41]. Residual neural networks allow the n^{th} layer access to the output of both the $(n-1)^{th}$ layer and the $(n-k)^{th}$ layer via a residual connection, where k is a positive integer (≥ 2).

In order to build the training input to the DUNE CVN three images of the neutrino interactions are produced, one for each of the three readout views, using the reconstructed hits on the individual wire planes. The images are not dependent on any further downstream reconstruction algorithms. The images contain 500 × 500 pixels, each in the (wire, time) parameter space, where the wire is the wire channel number and the time is the peak time of the reconstructed hit. The value of each pixel represents the integrated charge of the reconstructed hit. An example simulated 2.2 GeV ν_e CC interaction is shown in all three views in Figure 8 demonstrating the fine-grained detail available from the LArTPC technology.

The CVN is trained using approximately three million neutrino interactions from the Monte Carlo (MC) simulation. An independent sample is used to generate the physics measurement sensitivities. The training sample is chosen to ensure similar numbers of training examples from the different neutrino flavors. Validation is performed to ensure that similar classification performance is obtained for the training and test samples, i.e., to ensure that the CVN is not overtrained.

For the analysis presented here, we have used the primary output of the CVN, which returns probabilities that each interaction is one of the following classes: ν_μ CC, ν_e CC, ν_τ CC and NC. The ν_e CC probability distribution, $P(\nu_e$ CC), and the ν_μ CC probability distribution, $P(\nu_\mu$ CC), are shown in Figure 9. Excellent separation between the signal and background interactions is seen in both cases. The event selection requirement for an interaction to be included in the ν_e CC (ν_μ CC) is $P(\nu_e$ CC$) > 0.85$ ($P(\nu_\mu$ CC$) > 0.5$), optimized to produce the best sensitivity to observation of CP violation. Since all of the flavor classification probabilities must sum to one, the interactions selected in the two event selections are completely independent. The same selection criteria are used for both FHC and RHC beam modes.

Figure 10 shows the efficiency as a function of reconstructed energy (under the electron neutrino hypothesis) for the ν_e event selection. The efficiency in both the FHC and RHC beam modes exceeds 90% in the neutrino flux peak. Figure 11 shows the corresponding selection efficiency for the ν_μ event selection.

The ability of the CVN to identify neutrino flavor is dependent on its ability to resolve and identify the charged lepton. Backgrounds are induced by mis-identification of charged pions for ν_μ disappearance, and photons for ν_e appearance samples. Efficiency for these backgrounds corresponds directly with the momentum and isolation of the energy depositions from the pions and photons. Efficiency was also observed to drop as a function of track/shower angle when energy depositions aligned with wire planes. The shapes of the efficiency functions in lepton momentum, lepton angle, and hadronic energy fraction (inelasticity) were all observed to be consistent with results from previous studies, including hand scans of LArTPC simulations. It is conceivable that the efficacy is increased, especially at low charged lepton momentum, by the CVN identifying fine details of model

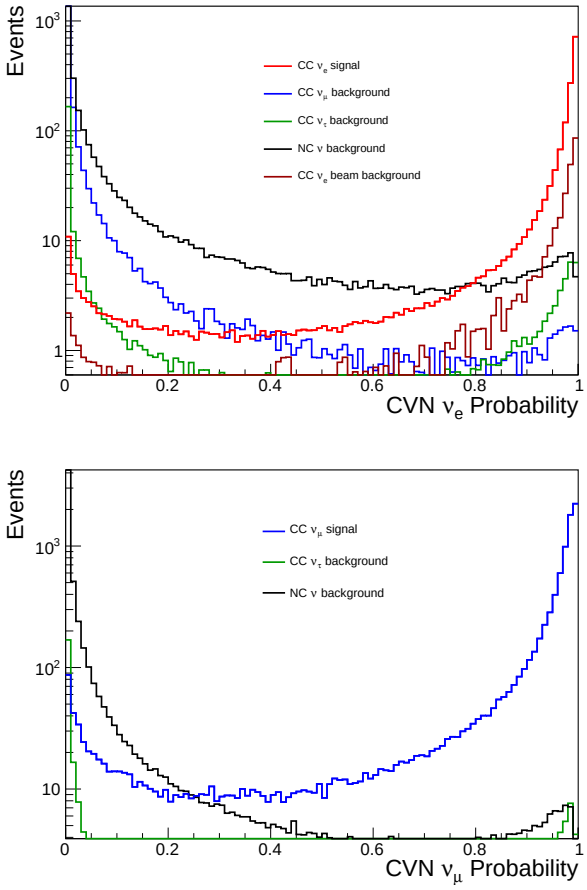

FIG. 9: The CVN ν_e CC probability (top) and ν_μ CC probability (bottom) for the FHC beam mode shown with a log scale.

dependent event kinematics. However, these effects are small enough to be covered by the assigned uncertainties.

VI. EXPECTED FAR DETECTOR EVENT RATE AND OSCILLATION PARAMETERS

The signal for ν_e ($\bar{\nu}_e$) appearance is an excess of CC ν_e and $\bar{\nu}_e$ interactions over the expected background in the far detector. The background to ν_e appearance is composed of: (1) CC interactions of ν_e and $\bar{\nu}_e$ intrinsic to the beam; (2) misidentified NC interactions; (3) misidentified ν_μ and $\bar{\nu}_\mu$ CC interactions; and (4) ν_τ and $\bar{\nu}_\tau$ CC interactions in which the τs decay leptonically into electrons/positrons. NC and ν_τ backgrounds emanate from interactions of higher-energy neutrinos that feed down to lower reconstructed neutrino energies due to missing energy in unreconstructed final-state neutrinos. The selected NC and CC ν_μ generally include an asymmetric decay of a relatively high energy π^0 coupled with a prompt photon conversion.

A full simulation chain that includes the beam flux, the GENIE neutrino interaction generator [42], and Geant4-based detector models has been implemented. Section II describes the beam design, simulated flux, and associated uncertainties. Event rates are based on a 1.2 MW neutrino beam and corresponding protons-on-target per year assumed to be 1.1 $\times 10^{21}$ POT. These numbers assume a combined uptime and efficiency of the Fermilab accelerator complex and the LBNF beamline of 56%. An upgrade to 2.4 MW is assumed after six years of data collection. The neutrino interaction model has been generated using GENIE 2.12 and the choices of models and tunes as well as associated uncertainties are described in detail in Section III. The performance parameters for the near and far detectors are described in detail in Sections IV and V. Near Detector Monte Carlo has been generated using Geant4 and a parameterized reconstruction based on true energy deposits in the active detector volumes has been used as described in Section IV. Far detector Monte Carlo has been generated using LArSoft and the reconstruction and event selection in the Far Detector has been fully implemented, as described in Section V.

The neutrino oscillation parameters and the uncertainty on those parameters are taken from the NuFIT 4.0 [4, 43] global fit to neutrino data; the values are given in Table VI. (See also [5] and [6] for other recent global fits.) The sensitivities in this chapter are shown assuming normal ordering; this is an arbitrary choice for simplicity of presentation.

Event rates are presented as a function of calendar years and are calculated with the following assumed deployment plan, which is based on a technically limited schedule.

- Start of beam run: Two FD module volumes for total fiducial mass of 20 kt, 1.2 MW beam
- After one year: Add one FD module volume for total fiducial mass of 30 kt
- After three years: Add one FD module volume for total fiducial mass of 40 kt
- After six years: Upgrade to 2.4 MW beam

Figures 12 and 13 show the expected rate of selected events for ν_e appearance and ν_μ disappearance, respectively, including expected flux, cross section, and oscillation probabilities, as a function of reconstructed neutrino energy at a baseline of 1285 km. The spectra are shown for a 3.5 year (staged) exposure each for neutrino and antineutrino beam mode, for a total run time of seven years. Tables VII and VIII give the integrated rate for the ν_e appearance and ν_μ disappearance spectra, respectively.

VII. DETECTOR UNCERTAINTIES

Detector effects impact the event selection efficiency as well as the reconstruction of quantities used in the oscillation fit, such as neutrino energy. The main sources of

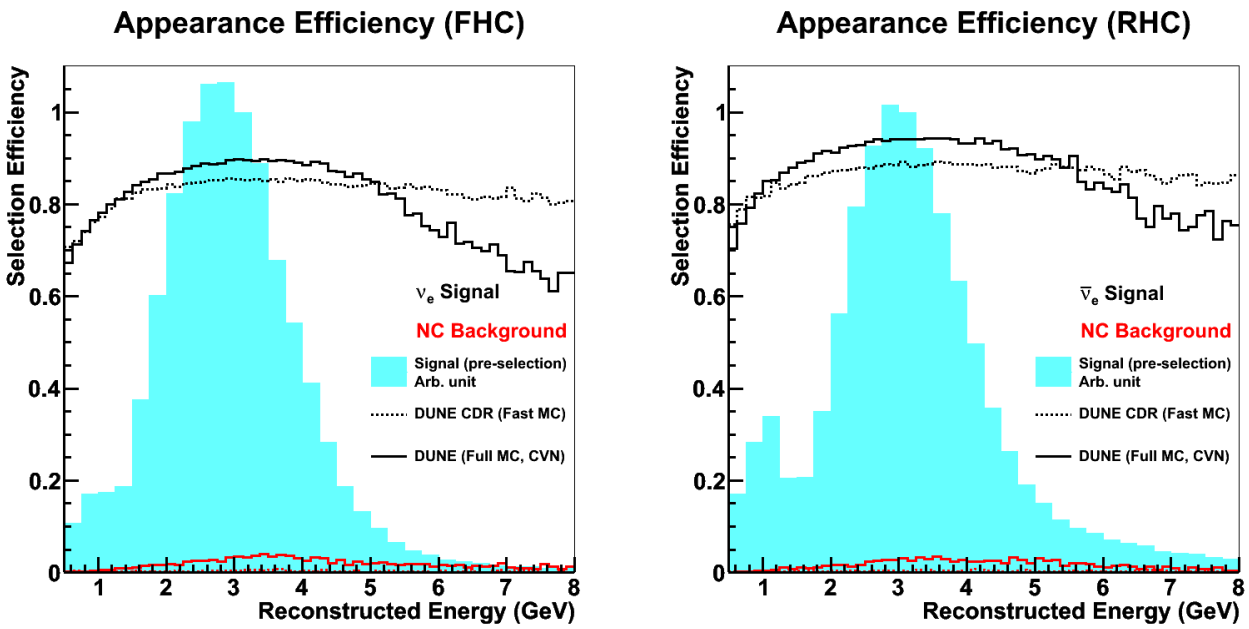

FIG. 10: The ν_e CC selection efficiency for FHC-mode (left) and RHC-mode (right) simulation with the criterion $P(\nu_e \text{ CC}) > 0.85$. The solid (dashed) lines show results from the CVN (CDR) for signal ν_e CC and $\bar{\nu}_e$ CC events in black and NC background interaction in red. The blue region shows the oscillated flux (A.U.) to illustrate the most important regions of the energy distribution.

Parameter	Central Value	Relative Uncertainty
θ_{12}	0.5903	2.3%
θ_{23} (NO)	0.866	4.1%
θ_{23} (IO)	0.869	4.0%
θ_{13} (NO)	0.150	1.5%
θ_{13} (IO)	0.151	1.5%
Δm^2_{21}	7.39×10^{-5} eV^2	2.8%
Δm^2_{32} (NO)	2.451×10^{-3} eV^2	1.3%
Δm^2_{32} (IO)	-2.512×10^{-3} eV^2	1.3%

TABLE VI: Central value and relative uncertainty of neutrino oscillation parameters from a global fit [4, 43] to neutrino oscillation data. Because the probability distributions are somewhat non-Gaussian (particularly for θ_{23}), the relative uncertainty is computed using 1/6 of the 3σ allowed range from the fit, rather than the 1σ range. For θ_{23}, θ_{13}, and Δm^2_{31}, the best-fit values and uncertainties depend on whether normal mass ordering (NO) or inverted mass ordering (IO) is assumed.

detector systematic uncertainties are limitations of calibration and modeling of particles in the detector. While neutrino interaction uncertainties can also affect reconstruction, this section is focused on effects that arise from the detectors.

The near LArTPC detector uses a similar technology as the far detector, namely they are both LArTPCs. However, important differences lead to uncertainties that do not fully correlate between the two detectors. First, the readout technology is different, as the near LArTPC uses pixels as well as a different, modular photon detector. Therefore, the charge response to particle types (e.g., muons and protons) will be different between near and far due to differences in electronics readout, noise, and local effects like alignment. Second, the high-intensity environment of the ND complicates associating detached energy deposits to events, a problem which does not exist in the FD. Third, the calibration programs will be different. For example, the ND has a high-statistics calibration sample of through-going, momentum-analyzed muons from neutrino interactions in the upstream rock, which does not exist for the FD. Finally, the reconstruction efficiency will be inherently different due to the relatively small size of the ND. Containment of charged hadrons will be significantly worse at the ND, especially for events with energetic hadronic showers or with vertices near the edges of the fiducial volume. Detector systematic uncertainties in the GArTPC at the near site will be entirely uncorrelated to the FD.

An uncertainty on the overall energy scale is included in the analysis presented here, as well as particle response uncertainties that are separate and uncorrelated between four species: muons, charged hadrons, neutrons, and electromagnetic showers. In the ND, muons reconstructed by range in LAr and by curvature in MPD are

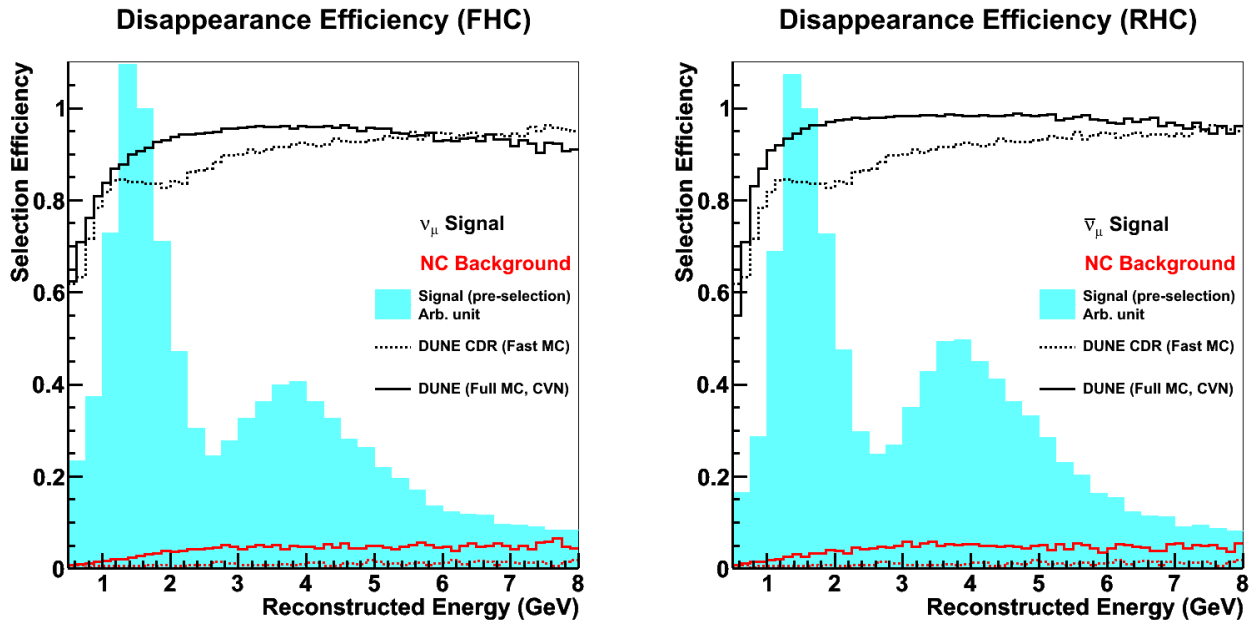

FIG. 11: The ν_μ CC selection efficiency for FHC-mode (left) and RHC-mode (right) simulation with the criterion $P(\nu_\mu \text{ CC}) > 0.5$. The solid (dashed) lines show results from the CVN (CDR) for signal ν_μ CC and $\bar{\nu}_\mu$ CC events in black and NC background interaction in red. The blue region shows the oscillated flux (A.U.) to illustrate the most important regions of the energy distribution.

treated separately. The energy scale and particle response uncertainties are allowed to vary with energy; each term is described by three free parameters:

$$E'_{rec} = E_{rec} \times (p_0 + p_1\sqrt{E_{rec}} + \frac{p_2}{\sqrt{E_{rec}}}) \qquad (2)$$

where E_{rec} is the nominal reconstructed energy, E'_{rec} is the shifted energy, and p_0, p_1, and p_2 are free fit parameters that are allowed to vary within *a priori* constraints. The energy scale and resolution parameters are conservatively treated as uncorrelated between the ND and FD. With a better understanding of the relationship between ND and FD calibration and reconstruction techniques, it may be possible to correlate some portion of the energy response. The full list of energy scale uncertainties is given as Table IX. Uncertainties on energy resolutions are also included and are taken to be 2% for muons, charged hadrons, and EM showers and 40% for neutrons.

The scale of these uncertainties is derived from recent experiments, including calorimetric based approaches (NOvA, MINERvA) and LArTPCs (LArIAT, MicroBooNE, ArgoNeuT). On NOvA [44], the muon (proton) energy scale achieved is $< 1\%$ (5%). Uncertainties associated to the pion and proton re-interactions in the detector medium are expected to be controlled from ProtoDUNE and LArIAT data, as well as the combined analysis of low density (gaseous) and high density (LAr) NDs. Uncertainties in the E field also contribute to the energy scale uncertainty, and calibration is needed (with cosmics at ND, laser system at FD) to constrain the overall energy scale. The recombination model will continue to be validated by the suite of LAr experiments and is not expected to be an issue for nominal field provided minimal E field distortions. Uncertainties in the electronics response are controlled with dedicated charge injection system and validated with intrinsic sources, Michel electrons and ^{39}Ar.

The response of the detector to neutrons is a source of active study and will couple strongly to detector technology. The validation of neutron interactions in LAr will continue to be characterized by dedicated measurements (e.g., CAPTAIN [45, 46]) and the LAr program (e.g., ArgoNeuT [47]). However, the association of the identification of a neutron scatter or capture to the neutrons true energy has not been demonstrated, and significant reconstruction issues exist, so a large uncertainty (20%) is assigned comparable to the observations made by MINERvA [48] assuming they are attributed entirely to the detector model. Selection of photon candidates from π^0 is also a significant reconstruction challenge, but a recent measurement from MicroBooNE indicates this is possible and the π^0 invariant mass has an uncertainty of 5%, although with some bias [49].

The ND and FD have different acceptance to CC events due to the very different detector sizes. The FD is sufficiently large that acceptance is not expected to vary significantly as a function of event kinematics. However, the ND selection requires that hadronic showers be well contained in LAr to ensure a good energy resolution, resulting in a loss of acceptance for events with en-

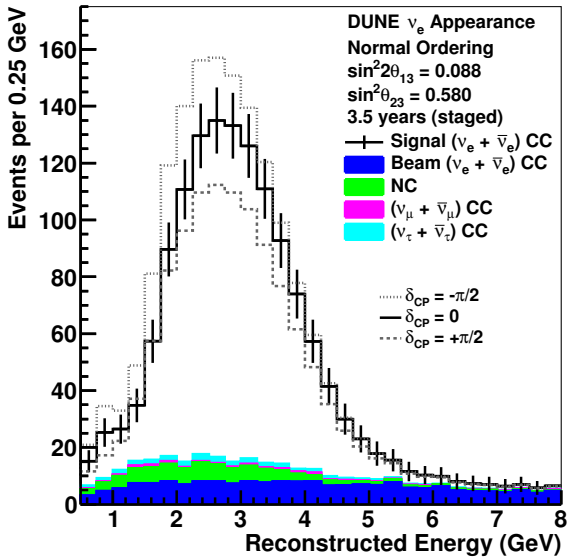

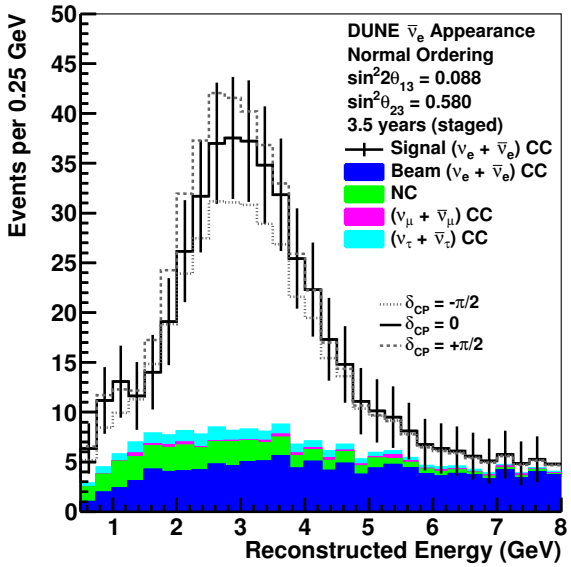

FIG. 12: ν_e and $\bar{\nu}_e$ appearance spectra: Reconstructed energy distribution of selected ν_e CC-like events assuming 3.5 years (staged) running in the neutrino-beam mode (top) and antineutrino-beam mode (bottom), for a total of seven years (staged) exposure. The plots assume normal mass ordering and include curves for $\delta_{\rm CP} = -\pi/2, 0$, and $\pi/2$.

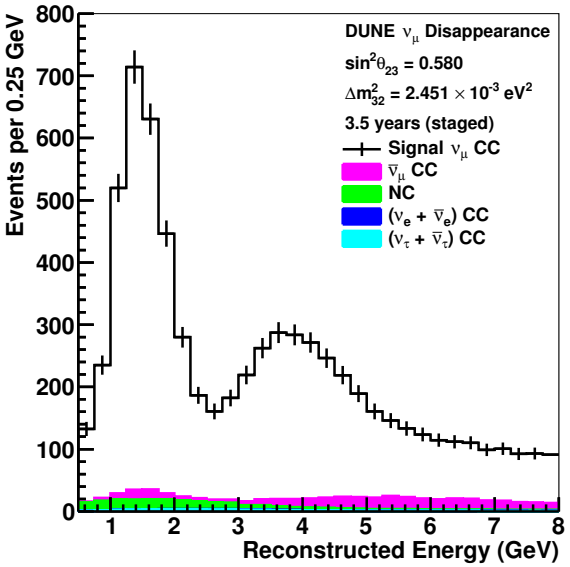

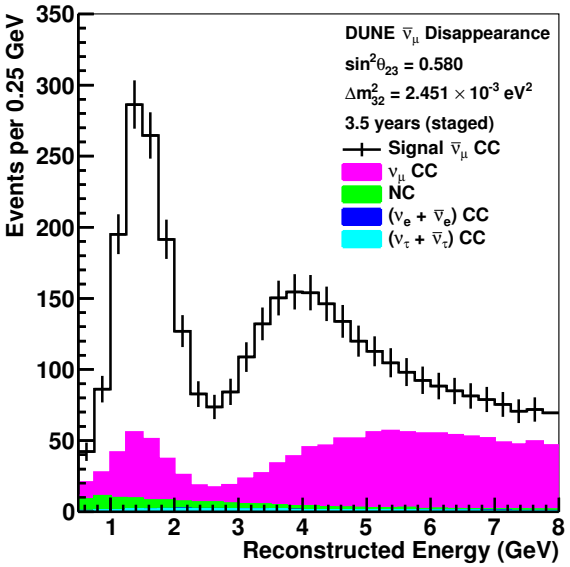

FIG. 13: ν_μ and $\bar{\nu}_\mu$ disappearance spectra: Reconstructed energy distribution of selected ν_μ CC-like events assuming 3.5 years (staged) running in the neutrino-beam mode (top) and antineutrino-beam mode (bottom), for a total of seven years (staged) exposure. The plots assume normal mass ordering.

ergetic hadronic showers. The ND also has regions of muon phase space with lower acceptance due to tracks exiting the side of the TPC but failing to match to the MPD.

Uncertainties are evaluated on the muon and hadron acceptance of the ND. The detector acceptance for muons and hadrons is shown in Figure 6. Inefficiency at very low lepton energy is due to events being misreconstructed as neutral current, which can also be seen in Figure 6. For high energy, forward muons, the inefficiency is only due to events near the edge of the fiducial volume where the muon happens to miss the MPD. At high transverse momentum, muons begin to exit the side of the LAr active volume, except when they happen to go along the 7 m axis. The acceptance is sensitive to the modeling of muons in the detector. An uncertainty is estimated based on the change in the acceptance as a function of muon kinematics. This uncertainty can be constrained with the MPD by comparing the muon spectrum in CC interac-

Sample	Expected Events (3.5 years staged)
ν mode	
ν_e Signal NO (IO)	1092 (497)
$\bar{\nu}_e$ Signal NO (IO)	18 (31)
Total Signal NO (IO)	1110 (528)
Beam $\nu_e + \bar{\nu}_e$ CC background	190
NC background	81
$\nu_\tau + \bar{\nu}_\tau$ CC background	32
$\nu_\mu + \bar{\nu}_\mu$ CC background	14
Total background	317
$\bar{\nu}$ mode	
ν_e Signal NO (IO)	76 (36)
$\bar{\nu}_e$ Signal NO (IO)	224 (470)
Total Signal NO (IO)	300 (506)
Beam $\nu_e + \bar{\nu}_e$ CC background	117
NC background	38
$\nu_\tau + \bar{\nu}_\tau$ CC background	20
$\nu_\mu + \bar{\nu}_\mu$ CC background	5
Total background	180

TABLE VII: ν_e and $\bar{\nu}_e$ appearance rates: Integrated rate of selected ν_e CC-like events between 0.5 and 8.0 GeV assuming a 3.5-year (staged) exposure in the neutrino-beam mode and antineutrino-beam mode. The signal rates are shown for both normal mass ordering (NO) and inverted mass ordering (IO), and all the background rates assume normal mass ordering. All the rates assume $\delta_{\rm CP} = 0$.

Sample	Expected Events (3.5 years staged)
ν mode	
ν_μ Signal	6200
$\bar{\nu}_\mu$ CC background	389
NC background	200
$\nu_\tau + \bar{\nu}_\tau$ CC background	46
$\nu_e + \bar{\nu}_e$ CC background	8
$\bar{\nu}$ mode	
$\bar{\nu}_\mu$ Signal	2303
ν_μ CC background	1129
NC background	101
$\nu_\tau + \bar{\nu}_\tau$ CC background	27
$\nu_e + \bar{\nu}_e$ CC background	2

TABLE VIII: ν_μ and $\bar{\nu}_\mu$ disappearance rates: Integrated rate of selected ν_μ CC-like events between 0.5 and 8.0 GeV assuming a 3.5-year (staged) exposure in the neutrino-beam mode and antineutrino-beam mode. The rates are shown for normal mass ordering and $\delta_{\rm CP} = 0$.

Particle Type	Allowed Variation In		
	p_0	p_1	p_2
all (except muons)	2%	1%	2%
μ (range)	2%	2%	2%
μ (curvature)	1%	1%	1%
p, $\pi^\pm$	5%	5%	5%
e, γ, π^0	2.5%	2.5%	2.5%
n	20%	30%	30%

TABLE IX: Uncertainties applied to the energy response of various particles. $p0$, p_1, and p_2 correspond to the constant, square root, and inverse square root terms in the energy response parameterization given in Equation 2. All are treated as uncorrelated between the ND and FD.

tions between the liquid and gaseous argon targets. The acceptance in the MPD is expected to be nearly 4π due to the excellent tracking and lack of scattering in the detector. Since the target nucleus is the same, and the two detectors are exposed to the same flux, the ratio between the two detectors is dominated by the LAr acceptance. Given the rate in the MPD, the expected constraint is at the level of ∼0.5% in the peak and ∼3% in the tail.

Inefficiency at high hadronic energy is due to the veto on more than 30 MeV deposited in the outer 30 cm collar of the active volume. Rejected events are typically poorly reconstructed due to low containment, and the acceptance is expected to decrease at high hadronic energy. Similar to the muon reconstruction, this acceptance is sensitive to detector modeling, and an uncertainty is evaluated based on the change in the acceptance as a function of true hadronic energy. This is more difficult to constrain with the MPD because of the uncertain mapping between true and visible hadronic energy in the LAr.

VIII. SENSITIVITY METHODS

Sensitivities to the neutrino mass ordering, CP violation, and θ_{23} octant, as well as expected resolution for neutrino oscillation parameter measurements, are obtained by simultaneously fitting the $\nu_\mu \to \nu_\mu$, $\bar{\nu}_\mu \to \bar{\nu}_\mu$, $\nu_\mu \to \nu_e$, and $\bar{\nu}_\mu \to \bar{\nu}_e$ far detector spectra along with selected samples from the near detector. It is assumed that 50% of the total exposure is in neutrino beam mode and 50% in antineutrino beam mode. A 50%/50% ratio of neutrino to antineutrino data has been shown to produce a nearly optimal $\delta_{\rm CP}$ and mass ordering sensitivity, and small deviations from this (e.g., 40%/60%, 60%/40%) produce negligible changes in these sensitivities.

In the sensitivity calculations, neutrino oscillation parameters governing long-baseline neutrino oscillation are allowed to vary. In all sensitivities presented here (unless otherwise noted) $\sin^2 2\theta_{13}$ is constrained by a Gaussian prior with 1σ width as given by the relative uncertainty shown in Table VI, while $\sin^2\theta_{23}$, Δm^2_{32}, and $\delta_{\rm CP}$ are allowed to vary freely. The oscillation parameters θ_{12} and Δm^2_{12} are allowed to vary constrained by the uncertainty in in Table VI. The matter density of the earth is allowed to vary constrained by a 2% uncertainty on its nominal value. Systematic uncertainty constraints from the near detector are included either by explicit inclusion of ND samples within the fit or by applying constraints expected from the ND data to FD-only fits.

Fits are performed using the analysis framework known as CAFAna [50], which was developed for the NOvA experiment and has been used for ν_μ-disappearance, ν_e-appearance, and joint fits, plus sterile neutrino searches and cross-section analyses. The compatibility of a particular oscillation hypothesis with the data is evaluated using the likelihood appropriate for Poisson-distributed data [51]:

$$\chi^2 = -2\log\mathcal{L} = 2\sum_i^{N_{\rm bins}}\left[M_i - D_i + D_i\ln\left(\frac{D_i}{M_i}\right)\right] + \sum_j^{N_{\rm systs}}\left[\frac{\Delta\vartheta_j}{\sigma_j}\right]^2 \quad (3)$$

where M_i is the MC expectation in bin i and D_i is the observed count. Most often the bins here represent reconstructed neutrino energy, but other observables, such as reconstructed kinematic variables or event classification likelihoods may also be used. Multiple samples with different selections can be fit simultaneously, as can multi-dimensional distributions of reconstructed variables.

Event records representing the reconstructed properties of neutrino interactions and, in the case of MC, the true neutrino properties are processed to fill the required histograms. Oscillated FD predictions are created by populating 2D histograms, with the second axis being the true neutrino energy, for each oscillation channel ($\nu_\alpha \to \nu_\beta$). These are then reweighted as a function of the true energy axis according to an exact calculation of the oscillation weight at the bin center and summed to yield the total oscillated prediction:

$$M_i = \sum_\alpha^{e,\mu}\sum_\beta^{e,\mu,\tau}\sum_j P_{\alpha\beta}(E_j)M_{ij}^{\alpha\beta} \quad (4)$$

where $P_{\alpha\beta}(E)$ is the probability for a neutrino created in flavor state α to be found in flavor state β at the FD. $M_{ij}^{\alpha\beta}$ represents the number of selected events in bin i of the reconstructed variable with true energy E_j, taken from a simulation where neutrinos of flavor α from the beam have been replaced by equivalent neutrinos in flavor β. Oscillation parameters that are not displayed in a given figure are profiled over using MINUIT [52]. That is, their values are set to those that produce the best match with the simulated data at each point in displayed parameter space.

Systematic uncertainties are included to account for the expected uncertainties in the beam flux, neutrino interaction, and detector response models used in the simulation at the time of the analysis. The neutrino interaction systematic uncertainties expand upon the existing GENIE systematic uncertainties to include recently exposed data/MC differences that are not expected to be resolved by the time DUNE starts running. The impact of systematic uncertainties is included by adding additional nuisance parameters into the fit. Each of these parameters can have arbitrary effects on the MC prediction, and can affect the various samples and channels within each sample in different ways. These parameters are profiled over in the production of the result. The range of these parameters is controlled by the use of Gaussian penalty terms to reflect our prior knowledge of reasonable variations.

For each systematic parameter under consideration, the matrices $M_{ij}^{\alpha\beta}$ are evaluated for a range of values of the parameter, by default $\pm1, 2, 3\sigma$. The predicted spectrum at any combination of systematic parameters can then be found by interpolation. Cubic interpolation is used, which guarantees continuous and twice-differentiable results, advantageous for gradient-based fitters such as MINUIT.

For many systematic variations, a weight can simply be applied to each event record as it is filled into the appropriate histograms. For others, the event record itself is modified, and for a few systematic uncertainties it is necessary to use an entirely separate sample that has been simulated with some alteration made to the simulation parameters.

Sensitivity calculations for CPV, neutrino mass ordering, and octant are performed, in addition to studies of oscillation parameter resolution in one and two dimensions. The experimental sensitivity and resolution functions are quantified using a test statistic, $\Delta\chi^2$, which is calculated by comparing the predicted spectra for alter-

Parameter	Prior	Range
$\sin^2\theta_{23}$	Uniform	[0.4; 0.6]
$\lvert\Delta m^2_{32}\rvert$ ($\times 10^{-3}$ eV^2)	Uniform	$\lvert$[2.3; 2.7]$\rvert$
$\delta_{\rm CP}$ (π)	Uniform	[-1;1]
θ_{13}	Gaussian	NuFIT 4.0

TABLE X: Treatment of the oscillation parameters for the simulated data set studies. The width of the θ_{13} range is determined from the NuFIT 4.0 result.

nate hypotheses. Where appropriate, a scan is performed over all possible values of $\delta_{\rm CP}^{true}$, and the neutrino mass ordering and the θ_{23} octant are also assumed to be unknown and are free parameters. The lowest value of $\Delta\chi^2$ is obtained by finding the combination of fit parameters that best describe the simulated data. The size of $\Delta\chi^2$ is a measure of how well those data can exclude this alternate hypothesis given the uncertainty in the model.

The expected resolution for oscillation parameters is determined from the spread in best-fit values obtained from an ensemble of data sets that vary both statistically and systematically. For each data set, the true value of each nuisance parameter is chosen randomly from a distribution determined by the a priori uncertainty on the parameter. For some studies, oscillation parameters are also randomly chosen as described in Table X. Poisson fluctuations are then applied to all analysis bins, based on the mean event count for each bin after the systematic adjustments have been applied. For each simulated data set in the ensemble, the test statistic is minimized, and the best-fit value of all parameters is determined. The one-sigma resolution is defined as the width of the interval around the true value containing 68% of simulated data sets.

The DUNE oscillation sensitivities presented here include four FD CC samples binned as a function of reconstructed neutrino energy: $\nu_\mu \to \nu_\mu$, $\overline{\nu_\mu} \to \overline{\nu_\mu}$, $\nu_\mu \to \nu_e$, and $\overline{\nu_\mu} \to \overline{\nu_e}$. Systematic parameters are constrained by unoscillated ND ν_μ and $\bar{\nu}_\mu$ CC samples selected from the LAr TPC and binned in two dimensions as a function of reconstructed neutrino energy (E_ν) and reconstructed Bjorken y (i.e. inelasticity).

Information from the ND, which is used to constrain systematic uncertainties, is included via additional χ^2 contributions (Equation 4) without oscillations. Detector uncertainties in the ND are included by adding a covariance matrix to the χ^2 calculation. This choice protects against overconstraining that could occur given the limitations of the parameterized ND reconstruction described in Section IV A taken together with the high statistical power at the ND. This covariance matrix is constructed with a many-universes technique. In each universe, all ND energy scale, resolution, and acceptance parameters are simultaneously thrown according to their respective uncertainties. The resulting spectra, in the same binning as is used in the oscillation sensitivity analysis, are compared with the nominal prediction to determine the bin-to-bin covariance.

CW: we should move the psotfit uncertainty plot here, and maybe add new plots whowing the size of the pre and post-fit uncertainties on some FD samples.

IX. SENSITIVITIES

Using the analysis framework described in the preceding sections, the simulated data samples for the far and near detectors are input to fits for CP violation sensitivity, mass ordering sensitivity, parameter measurement resolutions, and octant sensitivity. The results of these fits are presented in the following sections. Unless otherwise noted, all results include samples from both the near and far detectors and all systematic uncertainties are applied. Nominal exposures of seven, ten, and fifteen years are considered, where the staging plan described in Section VI, including a beam upgrade to 2.4 MW after six years, has been assumed. Results are shown as a function of the true values of oscillation parameters and/or as a function of exposure in staged years and/or kt-MW-years. In all cases, equal running in neutrino and antineutrino mode is assumed; no attempt is made to anticipate a realistic schedule of switching between neutrino and antineutrino mode. For the sake of simplicity, only true normal ordering is shown.

Possible variations of sensitivity are presented in several ways. For results at the nominal exposures, the sensitivity is calculated by performing fits in which the systematic parameters, oscillation parameters, and event rates are chosen at random, constrained in some cases by pre-fit uncertainties, as described in Section VIII. A fit is performed for each of these simulated data sets or "throws;" the nominal result is the median of these fit results and the uncertainty band is calculated to be the interval containing 68% of the fit results. For these results, the uncertainty band is drawn as as transparent filled area. In other cases, ranges of possible sensitivity results are explored by considering different true values of oscillation parameters or different analysis assumptions, such as removal of external constraints or variation in systematic uncertainties assumptions. For these results, a solid band indicates the range of possible results; this band is not intended to be interpreted as an uncertainty.

The exposures required to reach selected sensitivity milestones for the nominal analysis are summarized in Table XI.

Figure 14 shows the significance with which CP violation ($\delta_{\rm CP} \neq 0$ or π) can be observed as a function of the true value of $\delta_{\rm CP}$ for exposures corresponding to seven and ten years of data, with equal running in neutrino and antineutrino mode, using the staging scenario described in Section VI. This sensitivity has a characteristic double peak structure because the significance of a CPV measurement necessarily drops to zero where there

Physics Milestone	Exposure (staged years)
	$\sin^2\theta_{23} = 0.580$
5σ Mass Ordering	1
δ_{CP} = -$\pi/2$	
5σ Mass Ordering	2
100% of δ_{CP} values	
3σ CP Violation	3
δ_{CP} = -$\pi/2$	
3σ CP Violation	5
50% of δ_{CP} values	
5σ CP Violation	7
δ_{CP} = -$\pi/2$	
5σ CP Violation	10
50% of δ_{CP} values	
3σ CP Violation	13
75% of δ_{CP} values	
δ_{CP} Resolution of 10 degrees	8
$\delta_{CP} = 0$	
δ_{CP} Resolution of 20 degrees	12
δ_{CP} = -$\pi/2$	
$\sin^2 2\theta_{13}$ Resolution of 0.004	15

TABLE XI: Exposure in years, assuming true normal ordering and equal running in neutrino and antineutrino mode, required to reach selected physics milestones in the nominal analysis, using the NuFIT 4.0 best-fit values for the oscillation parameters. As discussed in Section **??**, there are significant variations in sensitivity with the value of $\sin^2\theta_{23}$, so the exact values quoted here are strongly dependent on that choice. The staging scenario described in Section VI is assumed. Exposures are rounded to the nearest year.

is no CPV: at the CP-conserving values of $-\pi$, 0, and π. The width of the transparent band represents 68% of fits when random throws are used to simulate statistical variations and select true values of the oscillation and systematic uncertainty parameters, constrained by pre-fit uncertainties. The solid curve is the median sensitivity. As illustrated in Section **??**, variation in the true value of $\sin^2\theta_{23}$ is responsible for a significant portion of this variation.

Figure 15 shows the significance with which CP violation can be determined for 75% and 50% of δ_{CP} values, and when $\delta_{CP} = -\pi/2$, as a function of exposure in years, using the staging scenario described in Section VI. It is

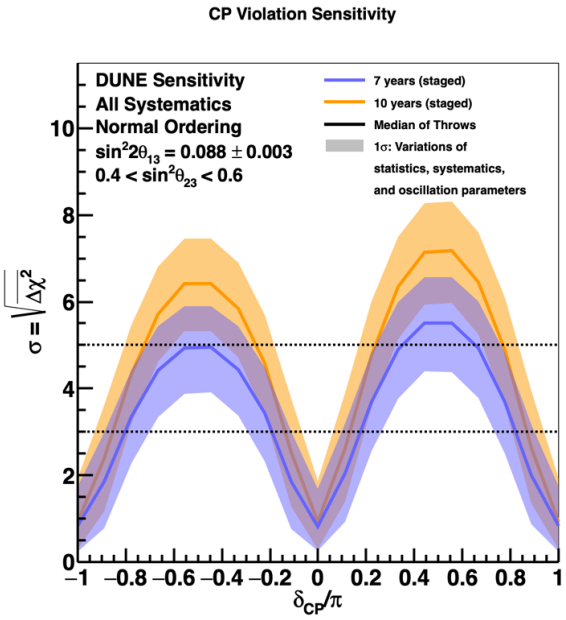

FIG. 14: Significance of the DUNE determination of CP-violation (i.e.: $\delta_{CP} \neq 0$ or π) as a function of the true value of δ_{CP}, for seven (blue) and ten (orange) years of exposure. True normal ordering is assumed. The width of the transparent bands cover 68% of fits in which random throws are used to simulate statistical variations and select true values of the oscillation and systematic uncertainty parameters, constrained by pre-fit uncertainties. The solid lines show the median sensitivity.

not possible for any experiment to provide 100% coverage in δ_{CP} for a CPV measurement because CPV effects vanish at certain values of δ_{CP}. The changes in trajectory of the curves in the first three years results from the staging of far detector module installation; the change at 6 years is due to the upgrade from 1.2- to 2.4-MW beam power. The width of the bands show the impact of applying an external constraint on $\sin^2 2\theta_{13}$. As seen in Table XI, CP violation can be observed with 5σ significance after about 7 years if $\delta_{CP} = -\pi/2$ and after about 10 years for 50% of δ_{CP} values. CP violation can be observed with 3σ significance for 75% of δ_{CP} values after about 13 years of running. Figure 16 shows the same CP violation sensitivity as a function of exposure in kt-MW-years. In the left plot, the width of the bands shows the impact of applying an external constraint on $\sin^2 2\theta_{13}$, while in the right plot, the width of the bands is the result of varying the true value of $\sin^2\theta_{23}$ within the NuFIT 4.0 90% C.L. allowed region.

Figure 17 shows the significance with which the neutrino mass ordering can be determined as a function of the true value of δ_{CP}, using the same exposures and staging assumptions described in the previous section. The characteristic shape results from near degeneracy between matter and CP-violating effects that occurs near $\delta_{CP} = \pi/2$ for true normal ordering. As in the CP violation sensitivity, the solid curve represents the median

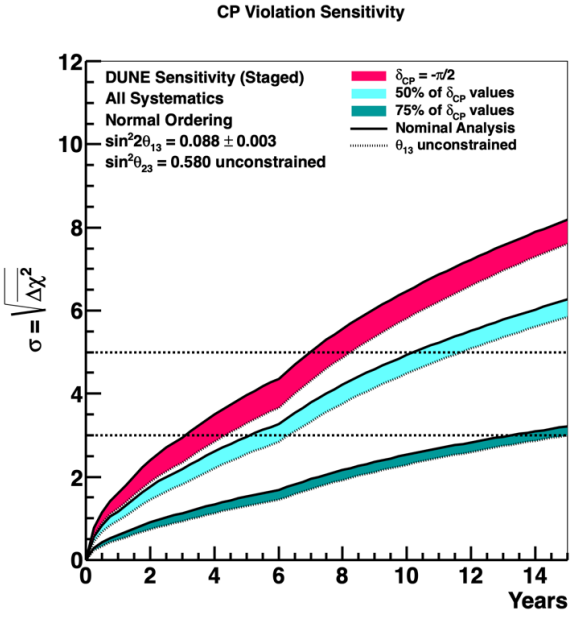

FIG. 15: Significance of the DUNE determination of CP-violation (i.e.: $\delta_{\rm CP} \neq 0$ or π) for the case when $\delta_{\rm CP} = -\pi/2$, and for 50% and 75% of possible true $\delta_{\rm CP}$ values, as a function of time in calendar years. True normal ordering is assumed. The width of the band shows the impact of applying an external constraint on $\sin^2 2\theta_{13}$.

sensitivity, the width of the transparent band represents 68% of fits when random throws are used to simulate statistical variations and select true values of the oscillation and systematic uncertainty parameters, constrained by pre-fit uncertainties, and variation in the true value of $\sin^2\theta_{23}$ is responsible for a significant portion of this variation.

Figure 18 shows the significance with which the neutrino mass ordering can be determined for 100% of $\delta_{\rm CP}$ values, and when $\delta_{\rm CP} = -\pi/2$, as a function of exposure in years. The width of the bands show the impact of applying an external constraint on $\sin^2 2\theta_{13}$. Figure 19 shows the same sensitivity as a function of exposure in kt-MW-years. As DUNE will be able to establish the neutrino mass ordering at the 5-σ level for 100% of $\delta_{\rm CP}$ values after between two and three years, these plots extend only to seven years and 500 kt-MW-years, respectively.

Studies have indicated that special attention must be paid to the statistical interpretation of neutrino mass ordering sensitivities [53, 54] because the $\Delta\chi^2$ metric does not follow the expected chi-squared function for one degree of freedom, so the interpretation of the sensitivity given by the Asimov data set is less straightforward. The error band on the mass ordering sensitivity shown in Figure 17 includes this effect using the technique of statistical throws described in Section **??**. The effect of statistical fluctuation and systematic uncertainties in the neutrino mass ordering sensitivity for values of $\sin^2\theta_{23}$ in

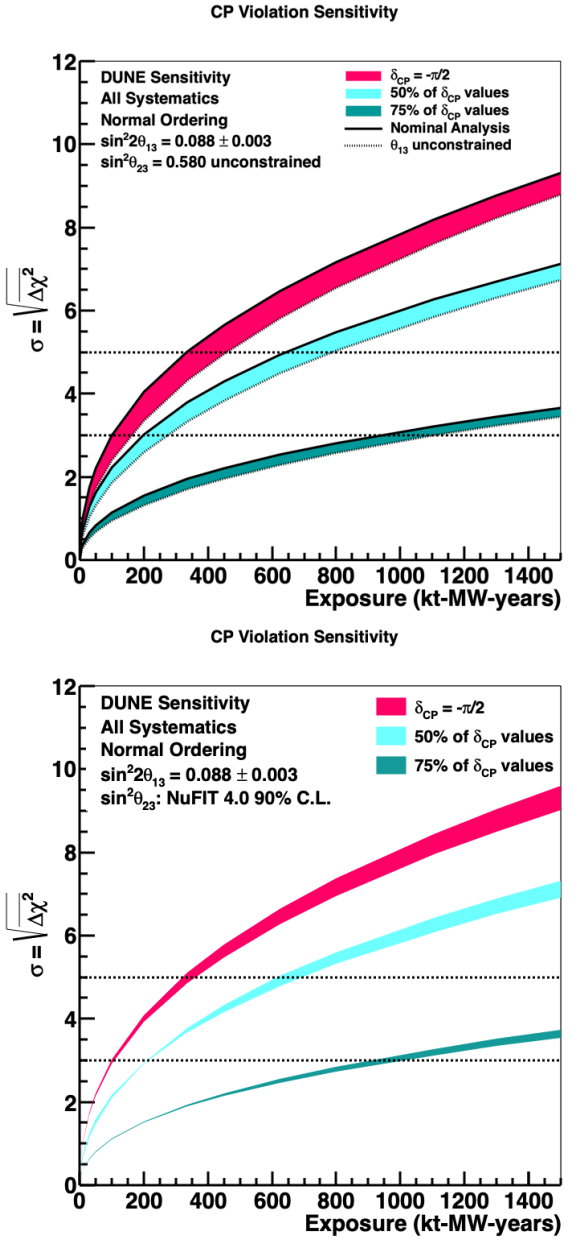

FIG. 16: Significance of the DUNE determination of CP-violation (i.e.: $\delta_{\rm CP} \neq 0$ or π) for the case when $\delta_{\rm CP} = -\pi/2$, and for 50% and 75% of possible true $\delta_{\rm CP}$ values, as a function of exposure in kt-MW-years. True normal ordering is assumed. Top: The width of the band shows the impact of applying an external constraint on $\sin^2 2\theta_{13}$. Bottom: The width of the band shows the impact of varying the true value of $\sin^2\theta_{23}$ within the NuFIT 4.0 90% C.L. region.

the range 0.56 to 0.60 is explored using random throws to determine the 1- and 2-σ ranges of possible sensitivity. The resulting range of sensitivities is shown in Figure 20, for 10 years of exposure.

In addition to the discovery potential for neutrino mass hierarchy and CPV, DUNE will improve the precision on key parameters that govern neutrino oscillations, includ-

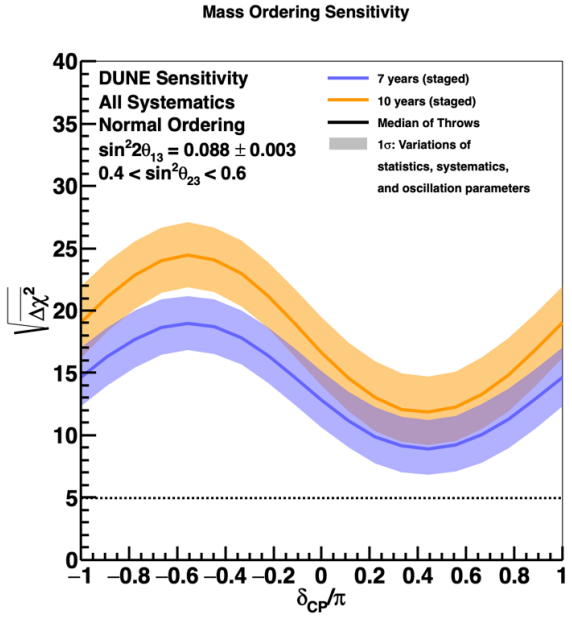

FIG. 17: Significance of the DUNE determination of the neutrino mass ordering, as a function of the true value of $\delta_{\rm CP}$, for seven (blue) and ten (orange) years of exposure. True normal ordering is assumed. The width of the transparent bands cover 68% of fits in which random throws are used to simulate statistical variations and select true values of the oscillation and systematic uncertainty parameters, constrained by pre-fit uncertainties. The solid lines show the median sensitivity.

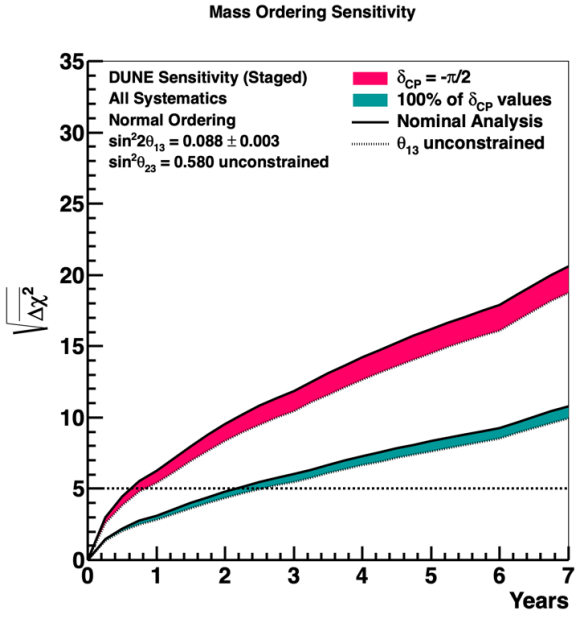

FIG. 18: Significance of the DUNE determination of the neutrino mass ordering for the case when $\delta_{\rm CP} = -\pi/2$, and for 100% of possible true $\delta_{\rm CP}$ values, as a function of time in calendar years. True normal ordering is assumed. The width of the band shows the impact of applying an external constraint on $\sin^2 2\theta_{13}$.

ing: $\delta_{\rm CP}$, $\sin^2 2\theta_{13}$, Δm^2_{31}, $\sin^2\theta_{23}$ and the octant of θ_{23}.

Figure 21 shows the resolution, in degrees, of DUNE's measurement of $\delta_{\rm CP}$, as a function of the true value of $\delta_{\rm CP}$. The resolution of this measurement is significantly better near CP-conserving values of $\delta_{\rm CP}$, compared to maximally CP-violating values. For fifteen years of exposure, resolutions between five and fifteen degrees are possible, depending on the true value of $\delta_{\rm CP}$. A smoothing algorithm has been applied to interpolate between values of $\delta_{\rm CP}$ at which the full analysis has been performed.

Figures 22 and 23 show the resolution of DUNE's measurements of $\delta_{\rm CP}$ and $\sin^2 2\theta_{13}$ and of $\sin^2 2\theta_{23}$ and Δm^2_{32}, respectively, as a function of exposure in kt-MW-years. As seen in Figure 21, the $\delta_{\rm CP}$ resolution varies significantly with the true value of $\delta_{\rm CP}$, but for favorable values, resolutions near five degrees are possible for large exposure. The DUNE measurement of $\sin^2 2\theta_{13}$ approaches the precision of reactor experiments for high exposure, allowing a comparison between the two results, which is of interest as a test of the unitarity of the PMNS matrix.

One of the primary physics goals for DUNE is the simultaneous measurement of all oscillation parameters governing long-baseline neutrino oscillation, without a need for external constraints. Figure 24 shows the 90% C.L. allowed regions for $\sin^2 2\theta_{13}$ and $\delta_{\rm CP}$ for 7, 10, and 15 years of running, when no external constraints are applied, compared to the current measurements from world data. Note that a degenerate lobe at higher values of $\sin^2 2\theta_{13}$ is present in the 7-year exposure, but is resolved for higher exposures. Figure 25 shows the two-dimensional allowed regions for $\sin^2\theta_{23}$ and $\delta_{\rm CP}$. Figure 26 explores the resolution sensitivity that is expected for values of $\sin^2\theta_{23}$ different from the NuFIT 4.0 central value. It is interesting to note that the lower exposure, opposite octant solutions for $\sin^2\theta_{23}$ are allowed at 90% C.L. in the absence of an external constraint on $\sin^2 2\theta_{13}$; however, at the 10 year exposure, this degeneracy is resolved by DUNE data without external constraint.

The measurement of $\nu_\mu \to \nu_\mu$ oscillations is sensitive to $\sin^2 2\theta_{23}$, whereas the measurement of $\nu_\mu \to \nu_e$ oscillations is sensitive to $\sin^2\theta_{23}$. A combination of both ν_e appearance and ν_μ disappearance measurements can probe both maximal mixing and the θ_{23} octant. Figure 27 shows the sensitivity to determining the octant as a function of the true value of $\sin^2\theta_{23}$.

The sensitivity results presented in the preceding sections assume that the true values of the parameters governing long-baseline neutrino oscillation are the central values of the NuFIT 4.0 global fit, given in Table VI. In this section, variations in DUNE sensitivity with other possible true values of the oscillation parameters are explored. Figures 28, 29, and 30 show DUNE sensitivity to CP violation and neutrino mass ordering when the true values of θ_{23}, θ_{13}, and Δm^2_{32}, respectively, vary within the 3σ range allowed by NuFIT 4.0. The largest effect

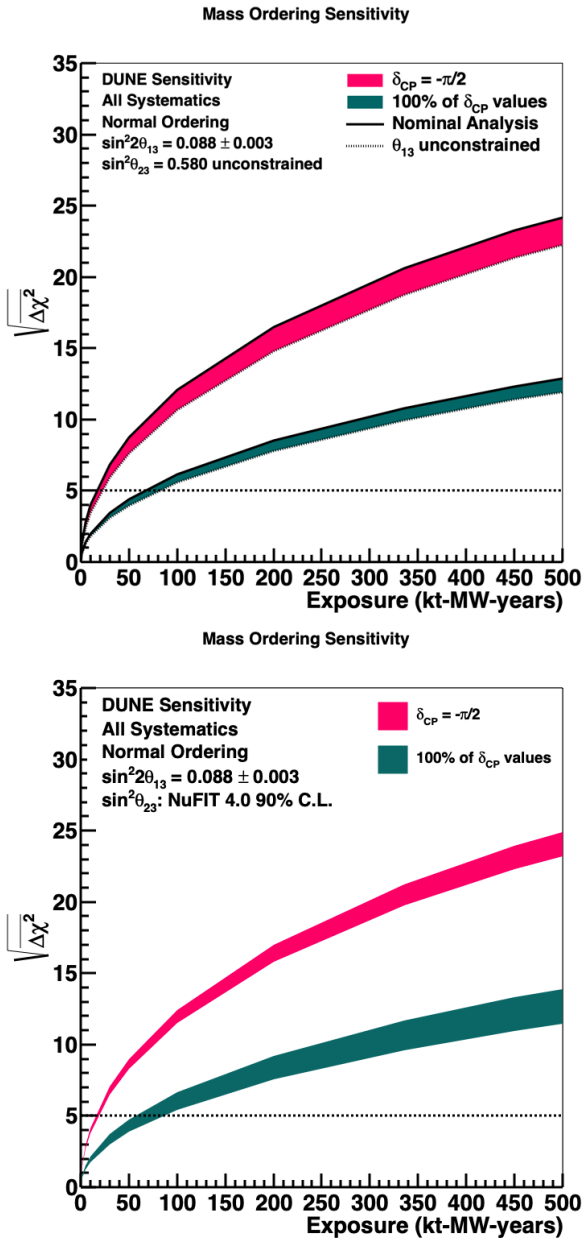

FIG. 19: Significance of the DUNE determination of the neutrino mass ordering for the case when $\delta_{\rm CP} = -\pi/2$, and for 100% of possible true $\delta_{\rm CP}$ values, as a function of exposure in kt-MW-years. True normal ordering is assumed. Top: The width of the band shows the impact of applying an external constraint on $\sin^2 2\theta_{13}$. Bottom: The width of the band shows the impact of varying the true value of $\sin^2\theta_{23}$ within the NuFIT 4.0 90% C.L. region.

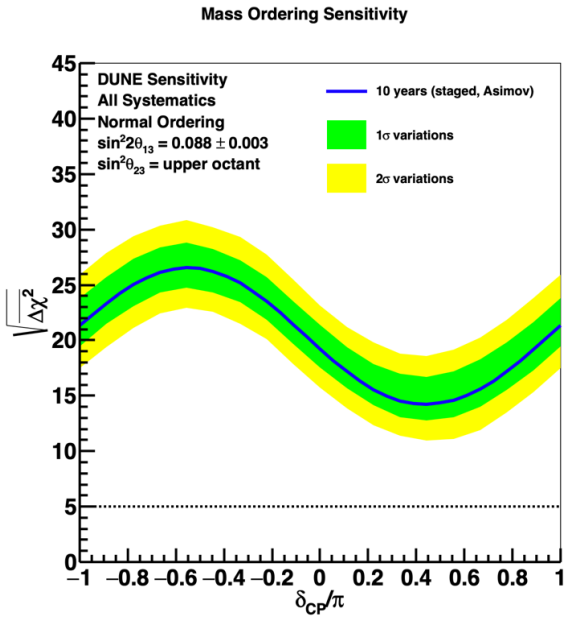

FIG. 20: Significance of the DUNE determination of the neutrino mass ordering, as a function of the true value of $\delta_{\rm CP}$, for ten years of exposure. True normal ordering is assumed. The width of the bands are 1- and 2-σ statistical and systematic variations. The blue curve shows sensitivity for the Asimov set.

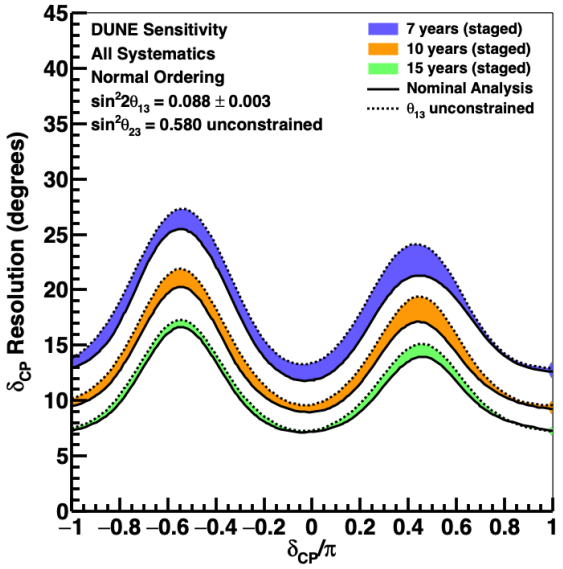

FIG. 21: Resolution in degrees for the DUNE measurement of $\delta_{\rm CP}$, as a function of the true value of $\delta_{\rm CP}$, for seven (blue), ten (orange), and fifteen (green) years of exposure. True normal ordering is assumed. The width of the band shows the impact of applying an external constraint on $\sin^2 2\theta_{13}$.

is the variation in sensitivity with the true value of θ_{23}, where degeneracy with $\delta_{\rm CP}$ and matter effects are significant. Values of θ_{23} in the lower octant lead to the best sensitivity to CP violation and the worst sensitivity to neutrino mass ordering, while the reverse is true for the upper octant. DUNE sensitivity for the case of maximal mixing is also shown. The true values of θ_{13} and Δm^2_{32} are highly constrained by global data and, within these constraints, do not have a dramatic impact on DUNE

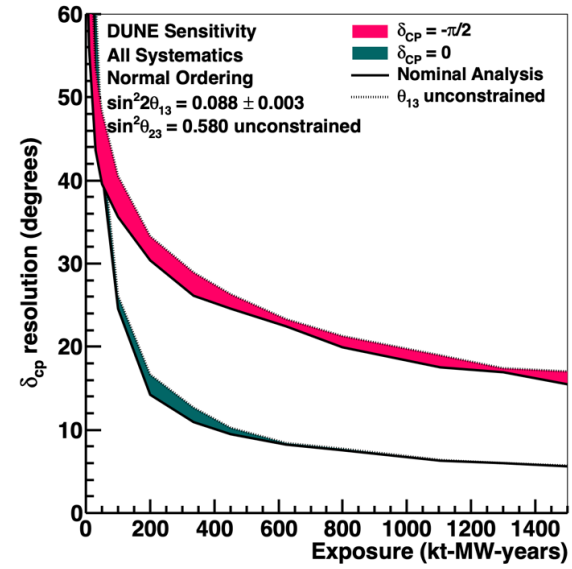

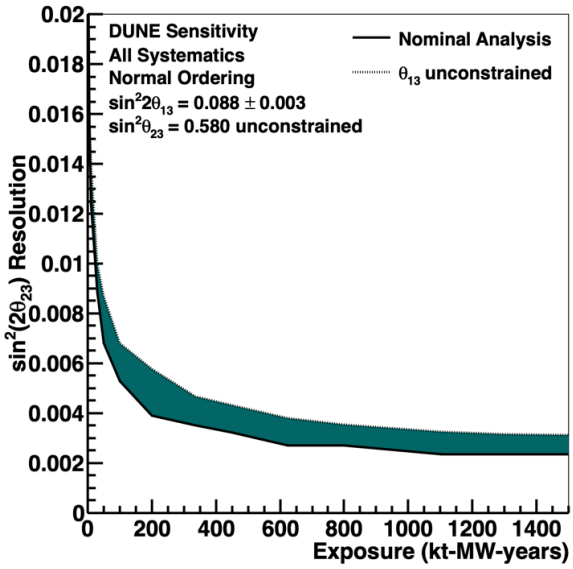

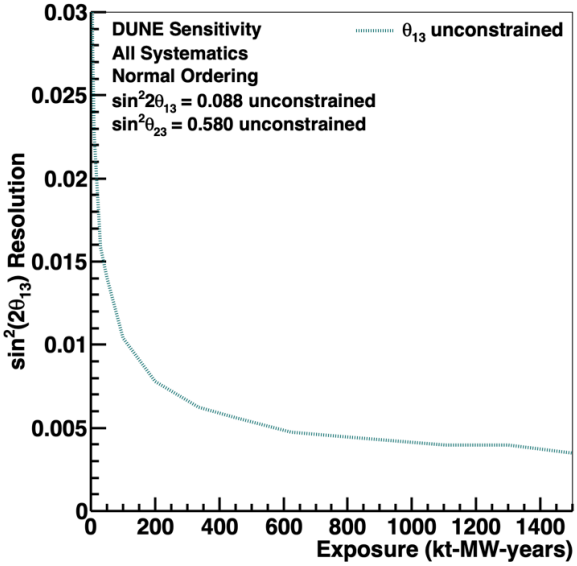

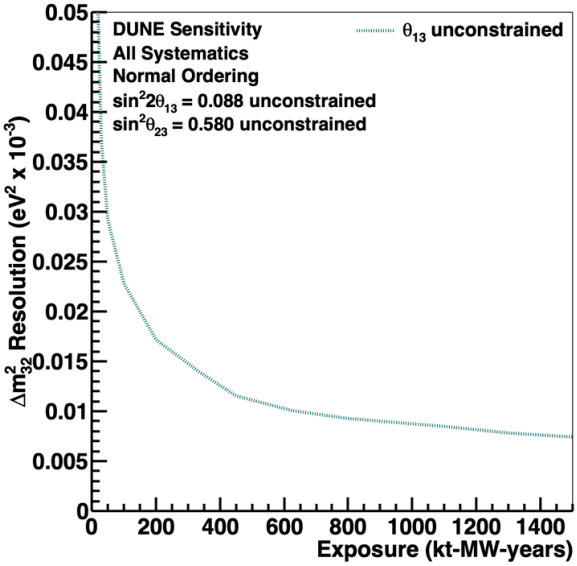

FIG. 22: Resolution of DUNE measurements of $\delta_{\rm CP}$ (top) and $\sin^2 2\theta_{13}$ (bottom), as a function of exposure in kt-MW-years. As seen in Figure 21, the $\delta_{\rm CP}$ resolution has a significant dependence on the true value of $\delta_{\rm CP}$, so curves for $\delta_{\rm CP} = -\pi/2$ (red) and $\delta_{\rm CP} = 0$ (green) are shown. The width of the band shows the impact of applying an external constraint on $\sin^2 2\theta_{13}$. For the $\sin^2 2\theta_{13}$ resolution, an external constraint does not make sense, so only the unconstrained curve is shown.

FIG. 23: Resolution of DUNE measurements of $\sin^2 2\theta_{23}$ (top) and Δm^2_{32} (bottom), as a function of exposure in kt-MW-years. The width of the band for the $\sin^2 2\theta_{23}$ resolution shows the impact of applying an external constraint on $\sin^2 2\theta_{13}$. For the Δm^2_{32} resolution, an external constraint does not have a significant impact, so only the unconstrained curve is shown.

sensitivity.

Implementation of systematic uncertainties in the nominal fits are described in Sections II, III, and VII. Prefit uncertainties on flux and cross section parameters are at the level of ∼10%. These uncertainties become constrained in the fit, especially by the ND. Figure 31 shows the level of constraint on each systematic parameter after the fit. The larger band shows the constraint that arises from the far detector alone, while the inner band shows the (much stronger) constraint from the near detector. The impact of adding the near detector is significant; flux and cross section parameters are very weakly constrained by the far detector alone. Parameters are implemented in such a way that there are no prefit correlations, but the constraints from the near detector cause parameters

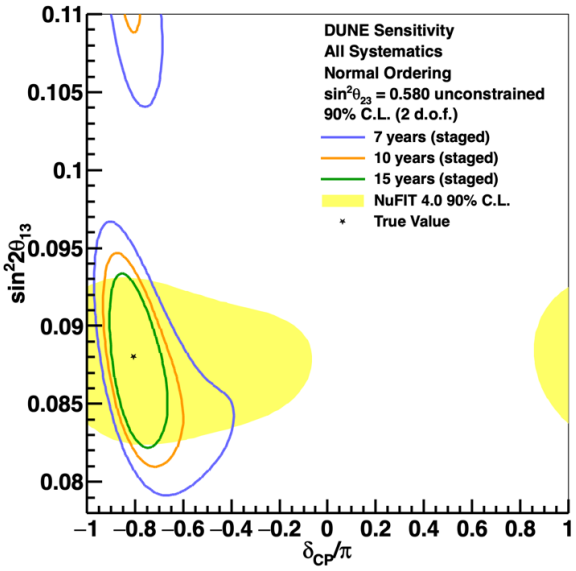

FIG. 24: Two-dimensional 90% C.L. region in $\sin^2 2\theta_{13}$ and $\delta_{\rm CP}$, for 7, 10, and 15 years of exposure, with equal running in neutrino and antineutrino mode. The 90% C. L. region for the NuFIT 4.0 global fit is shown in yellow for comparison. The true values of the oscillation parameters are assumed to be the central values of the NuFIT 4.0 global fit and the oscillation parameters governing long-baseline oscillation are unconstrained.

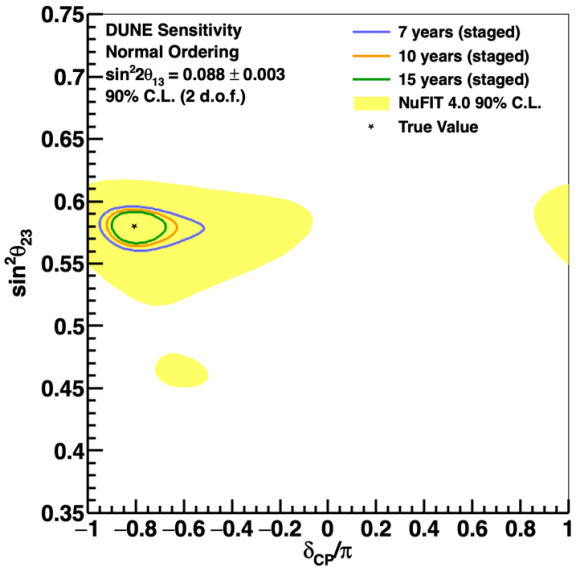

FIG. 25: Two-dimensional 90% C.L. region in $\sin^2\theta_{23}$ and $\delta_{\rm CP}$, for 7, 10, and 15 years of exposure, with equal running in neutrino and antineutrino mode. The 90% C. L. region for the NuFIT 4.0 global fit is shown in yellow for comparison. The true values of the oscillation parameters are assumed to be the central values of the NuFIT 4.0 global fit and $\sin^2 2\theta_{13}$ is constrained by NuFIT 4.0

to become correlated, which is not shown in the figure.

Some uncertainties are not reduced by the ND. For example, the energy scale parameters are treated as uncorrelated between detectors, so naturally the ND does not constrain them. Several important cross section uncertainties are not constrained by the near detector. In particular, an uncertainty on the ratio of ν_μ to ν_e cross sections is totally unconstrained. The most significant flux terms are constrained at the level of 20% of their *a priori* values. Less significant principal components have little impact on the observed distributions at either detector, and receive weaker constraints. Most cross section parameters that affect CC interactions are well constrained.

X. IMPACT OF THE NEAR DETECTOR

CW: This section should be drastically reduced, and be used to discuss possible short-comings, and the general approach to solving them. Here, we've taken the hard ND-sell from the TDR, which undermines the main thrust of this paper, and isn't really necessary... The oscillation sensitivity analysis presented in the previous section is intended to demonstrate the full potential of DUNE, with constraints from the full suite of near detectors described in introchnd?, including the LAr TPC, MPD, 3DST, and off-axis measurements. In addition to the ν_μ and $\bar{\nu}_\mu$ CC spectra used explicitly in this analysis, the LAr TPC is also expected to measure numerous exclusive final-state CC channels, including $1\pi^\pm$, $1\pi^0$, and multi-pion production. Measurements will be made as a function of other kinematic quantities in addition to reconstructed E_ν and y, such as four-momentum transfer to the nucleus, lepton angle, or final-state meson kinematics. The LAr TPC will also measure the sum of ν_e and $\bar{\nu}_e$ CC scattering, and NC events. Direct flux measurements will be possible with neutrino-electron elastic scattering, and the low-ν technique.

In addition to the many on-axis LAr samples, a complementary set of neutrino-argon measurements is expected from the HPG TPC. This detector will be sensitive to charged tracks at kinetic energies of just a few MeV, enabling the study of nuclear effects in unprecedented detail. It will also sign-select all charged particles, with nearly perfect pion-proton separation from dE/dx out to over 1 GeV/c momentum, so that high-purity measurements of CC1π^+ and CC1π^- are possible. It may be possible to directly measure neutron energy spectra from time of flight using the HPG TPC coupled to a high-performance ECAL. The 3DST-S will measure neutrino-carbon scattering and neutron production while ensuring excellent beam stability.

The LAr and MPD will also move off-axis to measure neutrino-argon interactions in many different fluxes. This will provide a direct constraint on the relationship

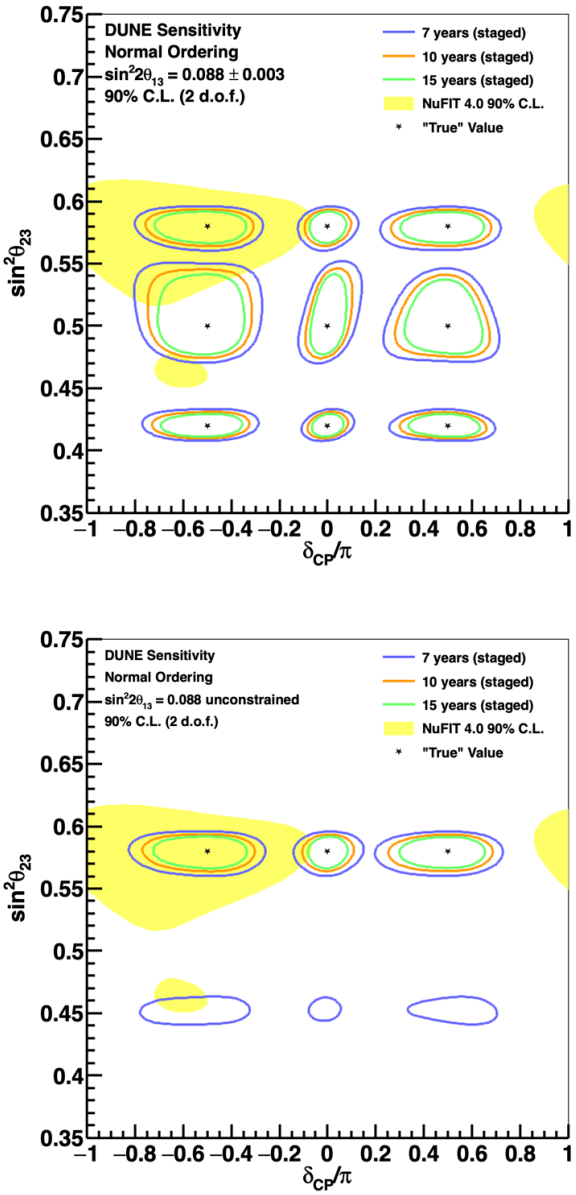

FIG. 26: Two-dimensional 90% C.L. region in $\sin^2\theta_{23}$ and $\delta_{\rm CP}$, for 7, 10, and 15 years of exposure, with equal running in neutrino and antineutrino mode. The 90% C.L. region for the NuFIT 4.0 global fit is shown in yellow for comparison. Several possible true values of the oscillation parameters, denoted by stars, are considered, and $\sin^2 2\theta_{13}$ is constrained (top) or unconstrained (bottom) by NuFIT 4.0. In the plot on the right, only one value for $\sin^2\theta_{23}$ is shown; without the constraint on $\sin^2 2\theta_{13}$, degenerate regions are allowed for lower exposures.

between neutrino energy and visible energy in LAr. By taking linear combinations of spectra at many off-axis positions, it is possible to reproduce the expected FD energy spectrum for a given set of oscillation parameters and directly measure visible energy.

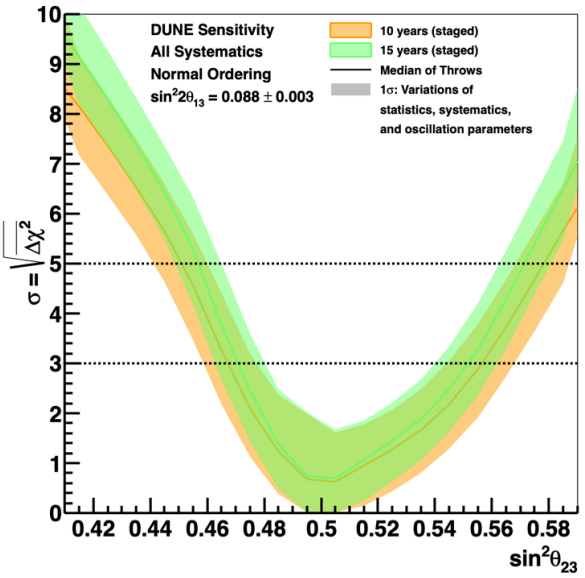

FIG. 27: Sensitivity to determination of the θ_{23} octant as a function of the true value of $\sin^2\theta_{23}$, for ten (orange) and fifteen (green) years of exposure. True normal ordering is assumed. The width of the transparent bands cover 68% of fits in which random throws are used to simulate statistical variations and select true values of the oscillation and systematic uncertainty parameters, constrained by pre-fit uncertainties. The solid lines show the median sensitivity.

The neutrino interaction model uncertainties shown in Section III represent our current knowledge of neutrino interactions, motivated by measurements wherever possible. The DUNE ND is able to constrain these uncertain parameters, as demonstrated in the previous section. However, due to the complexity of modeling neutrino-argon interactions, and the dearth of neutrino-argon measurements in the energy range relevant for DUNE, this is a necessary but insufficient condition for the ND program. There are possible variations to the interaction model that cannot be readily estimated, simply because we have yet to observe the inadequacy of the model. While these "unknown unknowns" are impossible to predict, guarding against them is critically important to the success of the DUNE physics program. For this reason, the ND is designed under the assumption that it must not only constrain some finite list of model parameters, but also be sensitive to general modeling deficiencies.

The sensitivity analysis presented in the previous section assumes the success of the ND program. Because of this assumption, in order to estimate the expected sensitivity without a ND, it is not sufficient to simply remove the on-axis LAr ND sample that is explicitly included in the analysis. We must also account for other potential biases from the interaction model, the "unknown unknowns." In this section, we consider two simple examples of bias, and evaluate the potential impact on oscil-

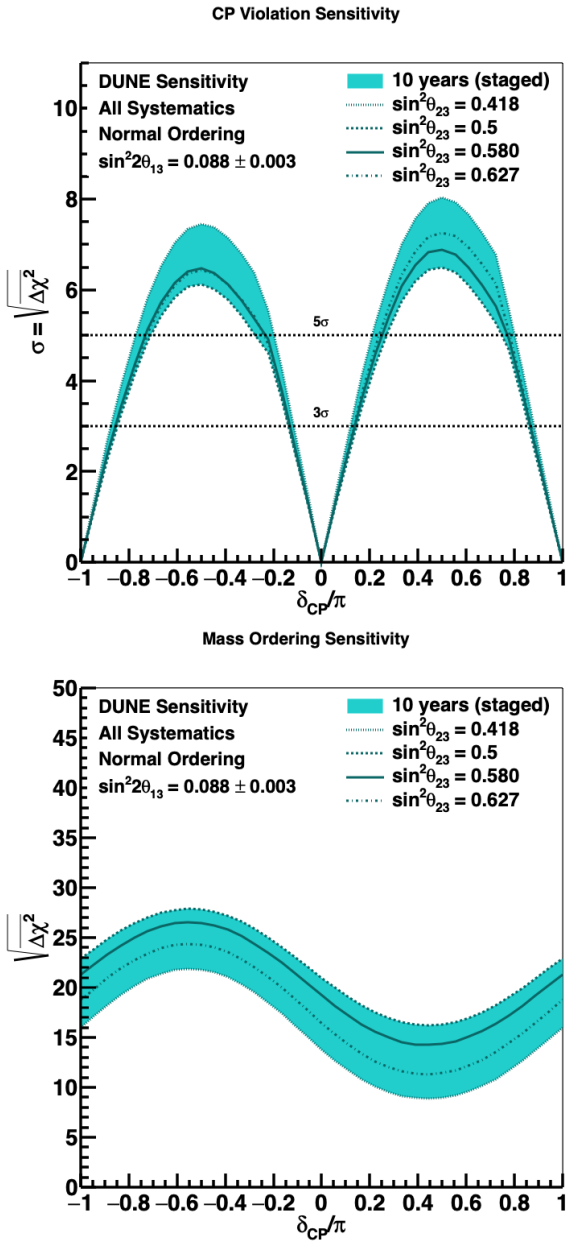

FIG. 28: Sensitivity to CP violation (top) and neutrino mass ordering (bottom), as a function of the true value of $\delta_{\rm CP}$, for 10 years of exposure, with equal running in neutrino and antineutrino mode. Curves are shown for true values of θ_{23} corresponding to the 3σ range of values allowed by NuFIT 4.0, as well as the NuFIT 4.0 central value and maximal mixing. The nominal sensitivity analysis is performed.

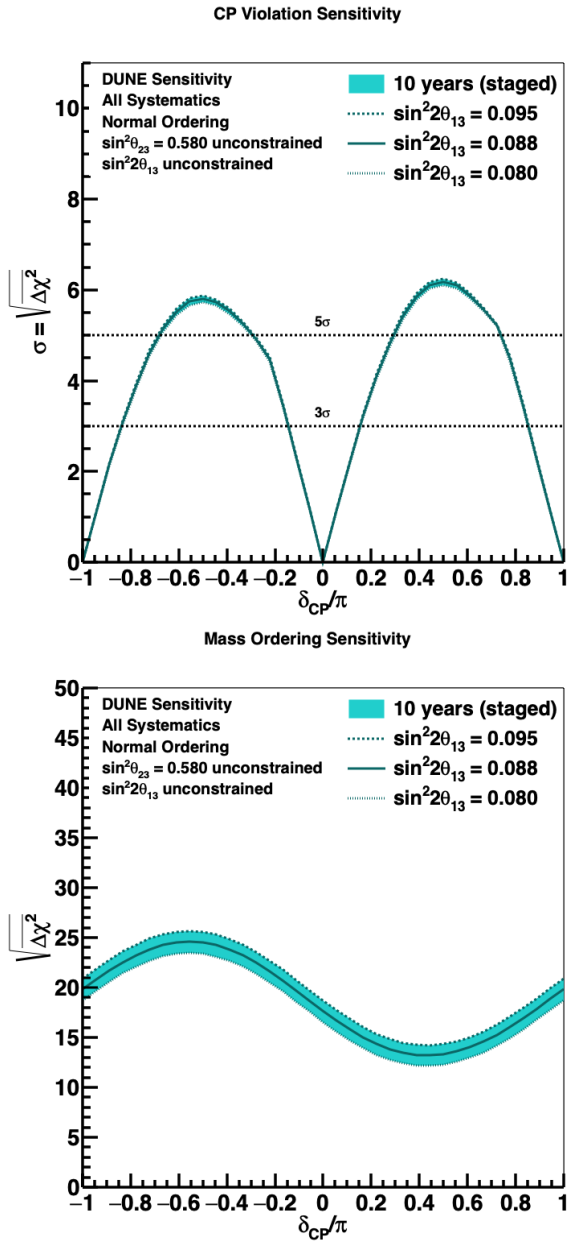

FIG. 29: Sensitivity to CP violation (top) and neutrino mass ordering (bottom), as a function of the true value of $\delta_{\rm CP}$, for 10 years of exposure, with equal running in neutrino and antineutrino mode. Curves are shown for true values of θ_{13} corresponding to the 3σ range of values allowed by NuFIT 4.0, as well as the NuFIT 4.0 central value. The nominal sensitivity analysis is performed, with the exception that θ_{13} is not constrained at the NuFit4.0 central value in the fit.

lation parameter measurements in a scenario where the ND capacity is reduced.

In one bias study, an alternative Monte Carlo sample is produced by reweighting the GENIE simulated events to NuWro. The objective of the reweighting is to reproduce the NuWro event spectra as a function of reconstructed neutrino energy, but without re-running the reconstruction. Eighteen true quantities that impact the reconstructed neutrino energy are identified: neutrino energy, lepton energy, lepton angle, Q^2, W, x, y, as well as the number and total kinetic energy carried by protons, neutrons, π^+, π^-, π^0, and the number of electromagnetic particles. A Boosted Decision Tree (BDT) is trained on vectors of these 18 quantities in GENIE and NuWro. The BDT minimizes a logistic loss function between GE-

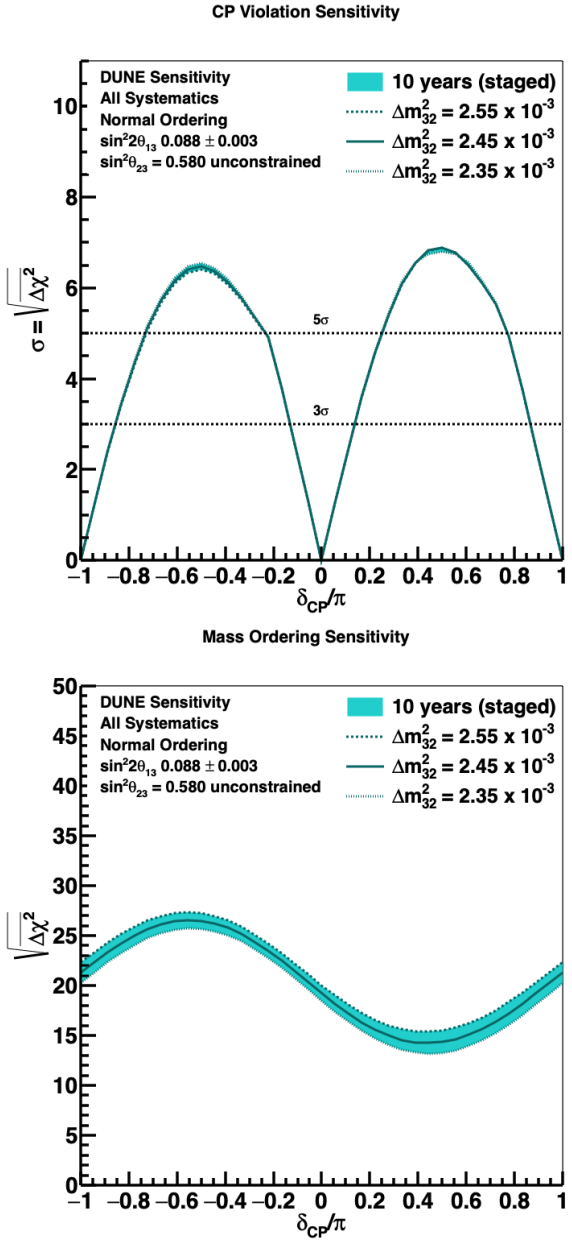

FIG. 30: Sensitivity to CP violation (top) and neutrino mass ordering (bottom), as a function of the true value of $\delta_{\rm CP}$, for 10 years of exposure, with equal running in neutrino and antineutrino mode. Curves are shown for true values of Δm^2_{32} corresponding to the 3σ range of values allowed by NuFIT 4.0, as well as the NuFIT 4.0 central value. The nominal sensitivity analysis is performed.

NIE and NuWro in the 18-dimensional space, producing a set of weights. When these weights are applied to GENIE events, the resulting event spectra match the NuWro spectra in all 18 quantities.

The resulting selected samples of FD ν_μ and ν_e CC events in FHC and RHC beam modes are fit using the nominal GENIE-based model and its uncertainties as described in Sections III and VII. The fit quality in the

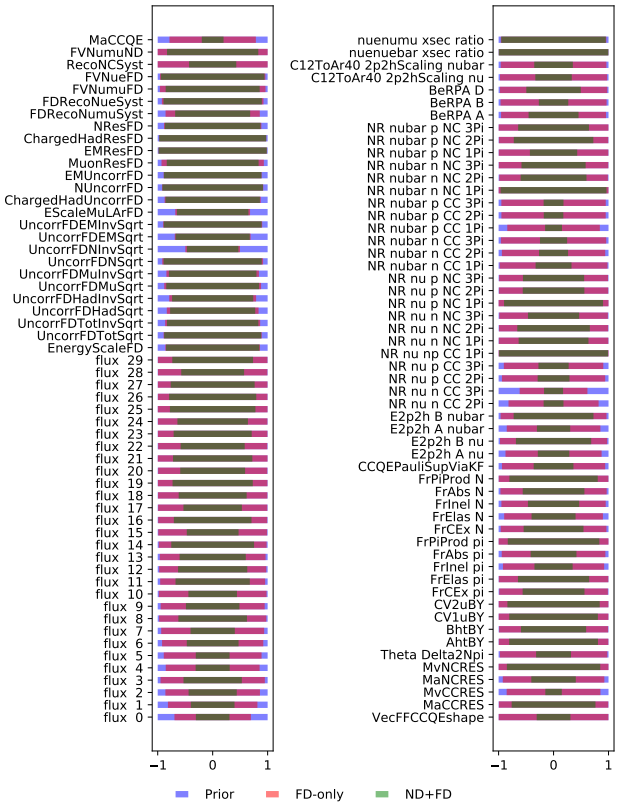

FIG. 31: The ratio of post-fit to pre-fit uncertainties for various systematic parameters for a 15-year staged exposure. The red band shows the constraint from the FD only in 15 years, while the green shows the ND+FD constraints.

FD-only scenario is high, with χ^2 per degree of freedom smaller than unity for all oscillation parameters. Systematic nuisance parameters are pulled from their best fit values by more than $\sim 0.6\sigma$.

The best-fit value of δ_{CP} is determined for the full range of possible true δ_{CP} values between $-\pi$ and $+\pi$. The difference between the best-fit and true values of δ_{CP} is found to be less than 14 degrees for 68% of the true values. To estimate the impact of such a bias on CP-violation sensitivity, an uncertainty equal to 14 degrees is added to the δ_{CP} resolution in quadrature. For a 10-year staged DUNE FD exposure, the resulting resolution is shown in the left panel of Figure 32 compared to the nominal sensitivity with the ND included. In the ND+FD (nominal) fit the bias is excluded, because in the ND the bias is easily detected and not attributable to oscillations. To estimate the sensitivity to non-zero CP violation as shown in the right panel of Figure 32, the nominal FD-only curve is reduced by the fractional increase in the δ_{CP} resolution at each point. The latter step is necessary because the uncertainty on δ_{CP} is not Gaussian.

As seen in Figure 32, the reduction in experimental sensitivity that would result from treating this example bias as a systematic uncertainty, which would be required

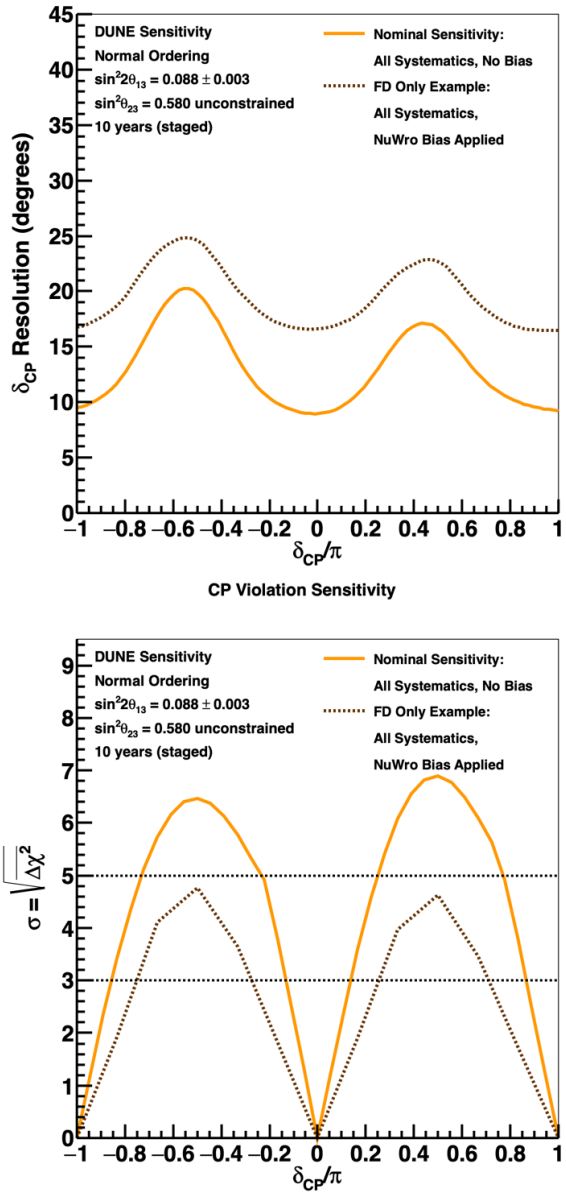

FIG. 32: The CP violation sensitivity for a FD-only scenario with an additional uncertainty added to cover the observed bias from one example variation. The δ_{CP} resolution (top) and CP violation sensitivity (bottom) are compared to the results from the nominal ND+FD analysis.

in the absence of near detector data, is dramatic. Many other reasonable variations of the neutrino interaction model are allowed by world data and would also have to be considered as potential sources of uncertainty without near detector data to observe and resolve model incompatibility.

As another example, we consider a possible deficiency of the GENIE model, specifically the case where the energy of final-state protons is reduced by 20%, with the energy going to neutrons instead. As neutrons are generally not observed, this will modify the relationship between neutrino energy and visible energy at the ND and FD. At the same time, the cross section model is altered so that the distribution of proton kinetic energy is unchanged. This alternate model is perfectly consistent with all available data; there is no reason to prefer our nominal GENIE model to this one.

By construction, this alternate model will not affect the fit at the on-axis near detector, as the cross section shift exactly cancels the loss in hadronic visible energy due to changing protons for neutrons. Nuisance parameters that affect the near detector spectra, namely flux and cross section uncertainties, are not pulled and remain at their nominal values with the same post-fit uncertainties observed in the Asimov sensitivity. At the far detector, however, the different neutrino energy spectrum leads to an observed shift in reconstructed energy with respect to the nominal prediction, visible in Figure 33.

Measured oscillation parameters returned by this fit are biased with respect to their true values. In particular, the best-fit values of Δm^2_{32} and $\sin^2\theta_{23}$ are significantly incorrect, as shown in Figure 34. Other parameters, including δ_{CP}, happen not to be pulled significantly from their true values by this particular model variation.

While the nominal model gives a good fit to the mock data in the on-axis ND, reconstructed spectra from off-axis ND data give a poor fit. This occurs because the cancellation between the cross section shift and the final-state proton-to-neutron ratio is dependent on the true neutrino energy spectrum. Off-axis data access different neutrino energy spectra, where the relationship is broken. By combining data at many off-axis positions, it is possible to produce a data-driven prediction of the expected FD flux for a given set of oscillation parameters, and directly compare this to the observation. Such a technique is not possible with solely on-axis ND data. This example demonstrates the importance of a capable ND, including the capability for off-axis measurements, to constrain not only the uncertain parameters of the interaction model, but also the physics in the model itself.

XI. CONCLUSION

The analyses presented here are based on full, end-to-end simulation, reconstruction, and event selection of FD Monte Carlo and parameterized analysis of ND Monte Carlo. Detailed uncertainties from flux, the neutrino interaction model, and detector effects have been included in the analysis. Sensitivity results are obtained using a sophisticated, custom fitting framework. These studies demonstrate that DUNE will be able to achieve its primary physics goals of measuring $\delta_{\rm CP}$ to high precision, unequivocally determining the neutrino mass ordering, and making precise measurements of the oscillation parameters governing long-baseline neutrino oscillation. It has also been demonstrated that accomplishing these goals relies upon accumulated statistics from

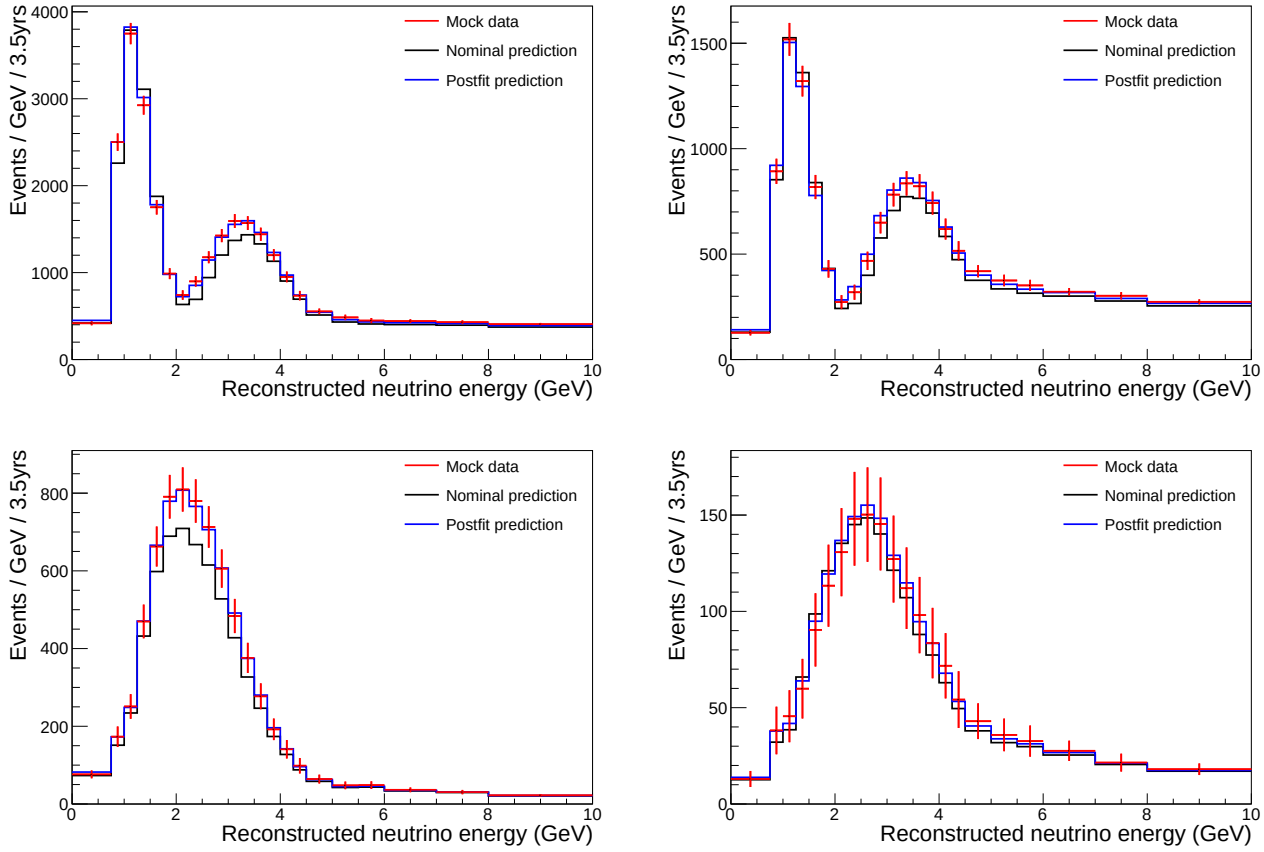

FIG. 33: Predicted distributions of reconstructed neutrino energy for selected ν_μ (top) and ν_e (bottom) events, in FHC (left) and RHC (right) beam modes in 7 years. The black curve shows the nominal GENIE prediction, while the red points are the mock data, where 20% of proton energy is shifted to neutrons. The blue curve is the post-fit result, where systematic and oscillation parameters are shifted to match the mock data. The ND spectra match the pre-fit prediction by construction and are not shown.

a well-calibrated, full-scale FD, operation of a 1.2-MW beam upgraded to 2.4 MW, and detailed analysis of data from a highly capable ND.

DUNE will be able to establish the neutrino mass ordering at the 5σ level for 100% of $\delta_{\rm CP}$ values after between two and three years. CP violation can be observed with 5σ significance after about 7 years if $\delta_{\rm CP} = -\pi/2$ and after about 10 years for 50% of $\delta_{\rm CP}$ values. CP violation can be observed with 3σ significance for 75% of $\delta_{\rm CP}$ values after about 13 years of running. For 15 years of exposure, $\delta_{\rm CP}$ resolution between five and fifteen degrees are possible, depending on the true value of $\delta_{\rm CP}$. The DUNE measurement of $\sin^2 2\theta_{13}$ approaches the precision of reactor experiments for high exposure, allowing measurements that do not rely on an external $\sin^2 2\theta_{13}$ constraint and facilitating a comparison between the DUNE and reactor $\sin^2 2\theta_{13}$ results, which is of interest as a potential signature for beyond the standard model physics. DUNE will have significant sensitivity to the θ_{23} octant for values of $\sin^2\theta_{23}$ less than about 0.47 and greater than about 0.55.

These measurements will make significant contributions to completion of the standard three-flavor mixing picture and guide theory in understanding if there are new symmetries in the neutrino sector or whether there is a relationship between the generational structure of quarks and leptons. Observation of CP violation in neutrinos would be an important step in understanding the origin of the baryon asymmetry of the universe. Precise measurements made in the context of the three-flavor paradigm may also yield inconsistencies that point us to physics beyond the standard three-flavor model.

[1] **DUNE** Collaboration, R. Acciarri *et al.*, "Long-Baseline Neutrino Facility (LBNF) and Deep Underground Neutrino Experiment (DUNE)," `arXiv:1601.05471 [physics.ins-det]`.

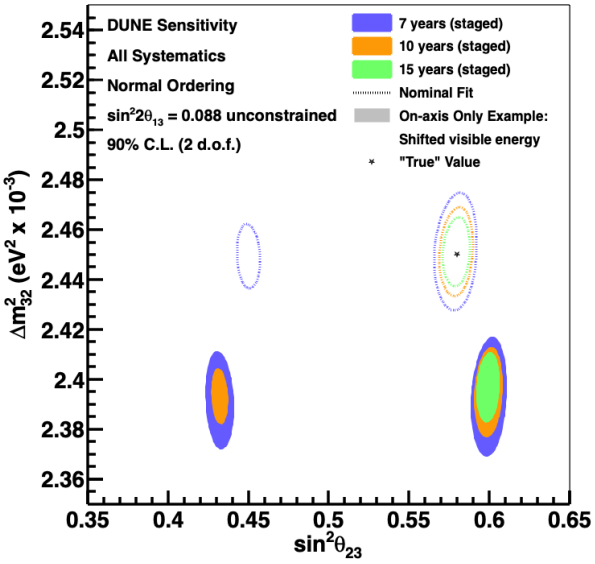

FIG. 34: Results of a fit to mock data where 20% of proton energy is shifted to neutrons. The true values of Δm^2_{32} and $\sin^2\theta_{23}$ are given by the star, while the allowed 90% C.L. regions are drawn around the best-fit point, for 7, 10, and 15 years of exposure. The solid region shows the result for a fit using the mock data, while the dashed curve shows the result for a fit using nominal simulation, for comparison.

[2] **DUNE** Collaboration, R. Acciarri *et al.*, "Long-Baseline Neutrino Facility (LBNF) and Deep Underground Neutrino Experiment (DUNE)," arXiv:1512.06148 [physics.ins-det].

[3] **DUNE** Collaboration, R. Acciarri *et al.*, "Long-Baseline Neutrino Facility (LBNF) and Deep Underground Neutrino Experiment (DUNE)," arXiv:1601.02984 [physics.ins-det].

[4] I. Esteban, M. C. Gonzalez-Garcia, A. Hernàndez-Cabezudo, M. Maltoni, and T. Schwetz, "Global analysis of three-flavour neutrino oscillations: synergies and tensions in the determination of $\theta_23, \delta_C P$, and the mass ordering," arXiv:1811.05487 [hep-ph].

[5] P. F. de Salas, D. V. Forero, C. A. Ternes, M. Tortola, and J. W. F. Valle, "Status of neutrino oscillations 2018: 3σ hint for normal mass ordering and improved CP sensitivity," *Phys. Lett.* **B782** (2018) 633–640, arXiv:1708.01186 [hep-ph].

[6] F. Capozzi, E. Lisi, A. Marrone, D. Montanino, and A. Palazzo, "Status and prospects of global analyses of neutrino mass-mixing parameters," *J. Phys. Conf. Ser.* **888** no. 1, (2017) 012037.

[7] **T2K** Collaboration, K. Abe *et al.*, "Search for CP Violation in Neutrino and Antineutrino Oscillations by the T2K Experiment with 2.2×10^{21} Protons on Target," *Phys. Rev. Lett.* **121** no. 17, (2018) 171802, arXiv:1807.07891 [hep-ex].

[8] **T2K** Collaboration, K. Abe *et al.*, "Constraint on the matter-antimatter symmetry-violating phase in neutrino oscillations," arXiv:1910.03887 [hep-ex].

[9] H. Nunokawa, S. J. Parke, and J. W. Valle, "CP Violation and Neutrino Oscillations," *Prog.Part.Nucl.Phys.* **60** (2008) 338–402, arXiv:0710.0554 [hep-ph].

[10] **LBNF/DUNE** Collaboration, P. Adamson *et al.*, "Long-Baseline Neutrino Facility (LBNF)/DUNE Conceptual Design Report: Annex 3A_opt." https://docs.dunescience.org/cgi-bin/private/RetrieveFile?docid=4559&filename=CDR_Optimized_Beam_Oct02.pdf&version=12, 2017.

[11] T. Vladisavljevic, "Constraining the T2K Neutrino Flux Prediction with 2009 NA61/SHINE Replica-Target Data," in *Proceedings, Prospects in Neutrino Physics (NuPhys2017): London, UK, December 20-22, 2017*, pp. 189–193. 2018. arXiv:1804.00272 [physics.ins-det].

[12] **NA61/SHINE Collaboration** Collaboration, A. Aduszkiewicz, "Report from the NA61/SHINE experiment at the CERN SPS," Tech. Rep. CERN-SPSC-2016-038. SPSC-SR-197, CERN, Geneva, Oct, 2016. https://cds.cern.ch/record/2222876.

[13] O. Benhar, A. Fabrocini, S. Fantoni, and I. Sick, "Spectral function of finite nuclei and scattering of GeV electrons," *Nucl. Phys.* **A579** (1994) 493–517.

[14] J. Nieves, J. E. Amaro, and M. Valverde, "Inclusive quasi-elastic neutrino reactions," *Phys. Rev.* **C70** (2004) 055503, arXiv:nucl-th/0408005 [nucl-th]. [Erratum: Phys. Rev.C72,019902(2005)].

[15] K. Gallmeister, U. Mosel, and J. Weil, "Neutrino-Induced Reactions on Nuclei," *Phys. Rev.* **C94** no. 3, (2016) 035502, arXiv:1605.09391 [nucl-th].

[16] V. Pandey, N. Jachowicz, T. Van Cuyck, J. Ryckebusch, and M. Martini, "Low-energy excitations and quasielastic contribution to electron-nucleus and neutrino-nucleus scattering in the continuum random-phase approximation," *Phys. Rev.* **C92** no. 2, (2015) 024606, arXiv:1412.4624 [nucl-th].

[17] J. E. Sobczyk, "Intercomparison of lepton-nucleus scattering models in the quasielastic region," *Phys. Rev.* **C96** no. 4, (2017) 045501, arXiv:1706.06739 [nucl-th].

[18] A. Bodek, "Removal and Binding Energies in Lepton Nucleus Scattering," arXiv:1801.07975 [nucl-th].

[19] J. Nieves, I. R. Simo, and M. J. V. Vacas, "Inclusive charged-current neutrino-nucleus reactions," *Phys. Rev. C* **83** (Apr, 2011) 045501, https://link.aps.org/doi/10.1103/PhysRevC.83.045501.

[20] R. Gran, J. Nieves, F. Sanchez, and M. J. V. Vacas, "Neutrino-nucleus quasi-elastic and 2p2h interactions up to 10 gev," *Phys. Rev. D* **88** (Dec, 2013) 113007, https://link.aps.org/doi/10.1103/PhysRevD.88.113007.

[21] M. Valverde, J. Amaro, and J. Nieves, "Theoretical uncertainties on quasielastic charged-current neutrinonucleus cross sections," *Physics Letters B* **638** no. 4, (2006) 325 – 332. http://www.sciencedirect.com/science/article/pii/S0370269306006344.

[22] F. Sanchez, "Private communication regarding RPA uncertainty parameterization.".

[23] R. Gran, "Model Uncertainties for Valencia RPA Effect for MINERvA," arXiv:1705.02932 [hep-ex].

[24] **T2K** Collaboration, K. Abe *et al.*, "Search for CP violation in Neutrino and Antineutrino Oscillations by the T2K experiment with 2.2×10^{21} protons on target," arXiv:1807.07891 [hep-ex].

[25] **MINERvA** Collaboration, P. A. Rodrigues *et al.*, "Identification of nuclear effects in neutrino-carbon interactions at low three-momentum transfer," *Phys. Rev. Lett.* **116** (2016) 071802, arXiv:1511.05944 [hep-ex].

[26] C. Colle, O. Hen, W. Cosyn, I. Korover, E. Piasetzky, J. Ryckebusch, and L. B. Weinstein, "Extracting the mass dependence and quantum numbers of short-range correlated pairs from $A(e, e'p)$ and $A(e, e'pp)$ scattering," *Phys. Rev.* **C92** no. 2, (2015) 024604, arXiv:1503.06050 [nucl-th].

[27] J. E. Amaro, M. B. Barbaro, J. A. Caballero, A. De Pace, T. W. Donnelly, G. D. Megias, and I. Ruiz Simo, "Density dependence of 2p-2h meson-exchange currents," *Phys. Rev.* **C95** no. 6, (2017) 065502, arXiv:1704.01539 [nucl-th].

[28] C. L. Smith, "Neutrino reactions at accelerator energies," *Physics Reports* **3** no. 5, (1972) 261 – 379, http://www.sciencedirect.com/science/article/pii/0370157372900105.

[29] C. Wilkinson, P. Rodrigues, S. Cartwright, L. Thompson, and K. McFarland, "Reanalysis of bubble chamber measurements of muon-neutrino induced single pion production," *Phys. Rev.* **D90** no. 11, (2014) 112017, arXiv:1411.4482 [hep-ex].

[30] P. Rodrigues, C. Wilkinson, and K. McFarland, "Constraining the GENIE model of neutrino-induced single pion production using reanalyzed bubble chamber data," *Eur. Phys. J.* **C76** no. 8, (2016) 474, arXiv:1601.01888 [hep-ex].

[31] **MINERvA** Collaboration, A. Mislivec *et al.*, "Measurement of total and differential cross sections of neutrino and antineutrino coherent $\pi^{\pm}$ production on carbon," *Phys. Rev.* **D97** no. 3, (2018) 032014, arXiv:1711.01178 [hep-ex].

[32] M. Sanchez, "Nova results and prospects," in *XXVIII International Conference on Neutrino Physics and Astrophysics (Neutrino 2018)*. Zenodo, June, 2018. https://zenodo.org/record/1286758.

[33] M. Day and K. S. McFarland, "Differences in quasielastic cross sections of muon and electron neutrinos," *Phys. Rev. D* **86** (Sep, 2012) 053003. http://link.aps.org/doi/10.1103/PhysRevD.86.053003.

[34] C. Andreopoulos, C. Barry, S. Dytman, H. Gallagher, T. Golan, R. Hatcher, G. Perdue, and J. Yarba, "The GENIE Neutrino Monte Carlo Generator: Physics and User Manual," arXiv:1510.05494 [hep-ph].

[35] J. Asaadi *et al.*, "A pixelated charge readout for Liquid Argon Time Projection Chambers," *JINST* **13** no. 02, (2018) C02008.

[36] A. Bross *et al.*, "High-Pressure Argon gas TPC Option for the DUNE Near Detector," DUNE doc 12388, 2019. https://docs.dunescience.org/cgi-bin/private/ShowDocument?docid=12388&asof=2019-7-15.

[37] L. Emberger and F. Simon, "A highly granular calorimeter concept for long baseline near detectors," *J. Phys. Conf. Ser.* **1162** no. 1, (2019) 012033, arXiv:1810.03677 [physics.ins-det].

[38] A. Radovic, M. Williams, D. Rousseau, M. Kagan, D. Bonacorsi, A. Himmel, A. Aurisano, K. Terao, and T. Wongjirad, "Machine learning at the energy and intensity frontiers of particle physics," *Nature* **560** no. 7716, (2018) 41–48.

[39] A. Aurisano, A. Radovic, D. Rocco, A. Himmel, M. D. Messier, E. Niner, G. Pawloski, F. Psihas, A. Sousa, and P. Vahle, "A Convolutional Neural Network Neutrino Event Classifier," *JINST* **11** no. 09, (2016) P09001, arXiv:1604.01444 [hep-ex].

[40] K. He, X. Zhang, S. Ren, and J. Sun, "Deep residual learning for image recognition," *CoRR* **abs/1512.03385** (2015) , arXiv:1512.03385. http://arxiv.org/abs/1512.03385.

[41] J. Hu, L. Shen, and G. Sun, "Squeeze-and-excitation networks," *CoRR* **abs/1709.01507** (2017) , arXiv:1709.01507. http://arxiv.org/abs/1709.01507.

[42] C. Andreopoulos *et al.*, "The GENIE Neutrino Monte Carlo Generator," *Nucl. Instrum. Meth.* **A614** (2010) 87–104, arXiv:0905.2517 [hep-ph].

[43] "Nufit4.0." http://www.nu-fit.org/.

[44] **NOvA** Collaboration, M. A. Acero *et al.*, "New constraints on oscillation parameters from ν_e appearance and ν_μ disappearance in the NOvA experiment," *Phys. Rev.* **D98** (2018) 032012, arXiv:1806.00096 [hep-ex].

[45] **CAPTAIN** Collaboration, H. Berns *et al.*, "The CAPTAIN Detector and Physics Program." 2013.

[46] **CAPTAIN** Collaboration, B. Bhandari *et al.*, "First Measurement of the Total Neutron Cross Section on Argon Between 100 and 800 MeV," arXiv:1903.05276 [hep-ex].

[47] **ArgoNeuT** Collaboration, R. Acciarri, C. Adams, J. Asaadi, B. Baller, T. Bolton, C. Bromberg, F. Cavanna, E. Church, D. Edmunds, A. Ereditato, S. Farooq, A. Ferrari, R. S. Fitzpatrick, B. Fleming, A. Hackenburg, G. Horton-Smith, C. James, K. Lang, M. Lantz, I. Lepetic, B. R. Littlejohn, X. Luo, R. Mehdiyev, B. Page, O. Palamara, B. Rebel, P. R. Sala, G. Scanavini, A. Schukraft, G. Smirnov, M. Soderberg, J. Spitz, A. M. Szelc, M. Weber, W. Wu, T. Yang, and G. P. Zeller, "Demonstration of mev-scale physics in liquid argon time projection chambers using argoneut," *Phys. Rev. D* **99** (Jan, 2019) 012002. https://link.aps.org/doi/10.1103/PhysRevD.99.012002.

[48] **MINERvA** Collaboration, M. Elkins *et al.*, "Neutron measurements from anti-neutrino hydrocarbon reactions," arXiv:1901.04892 [hep-ex].

[49] **MicroBooNE** Collaboration, C. Adams *et al.*, "First Measurement of ν_μ Charged-Current π^0 Production on Argon with a LArTPC," arXiv:1811.02700 [hep-ex].

[50] NOvA Collaboration, ed., *NOvA-ART*, ch. CAFAna overview. Redmine, 2019. https://cdcvs.fnal.gov/redmine/projects/novaart/wiki/CAFAna_overview.

[51] **Particle Data Group** Collaboration, M. Tanabashi *et al.*, "Review of Particle Physics," *Phys. Rev.* **D98** no. 3, (2018) 030001.

[52] F. James, "MINUIT Function Minimization and Error Analysis: Reference Manual Version 94.1." CERN-D-506, CERN-D506, 1994.

[53] X. Qian, A. Tan, W. Wang, J. Ling, R. McKeown, *et al.*, "Statistical Evaluation of Experimental Determinations of Neutrino Mass Hierarchy," *Phys.Rev.* **D86** (2012) 113011, arXiv:1210.3651 [hep-ph].

[54] M. Blennow, P. Coloma, P. Huber, and T. Schwetz, "Quantifying the sensitivity of oscillation experiments to the neutrino mass ordering," *JHEP* **1403** (2014) 028, arXiv:1311.1822 [hep-ph].

[55] E_{avail} is calorimetrically visible energy in the detector, roughly speaking total recoil hadronic energy, less the

masses of $\pi^{\pm}$ and the kinetic energies of neutrons